Materials Today Bio 30 (2025) 101387

Contents lists available at ScienceDirect

Materials Today Bio

journal homepage: www.journals.elsevier.com/materials-today-bio

AIEgen-self-assembled nanoparticles with anti-PD-L1 antibody functionalization realize enhanced synergistic photodynamic therapy and immunotherapy against malignant melanoma

Lu Li [a,1], Qing Xu [a,1], Xiuzhen Zhang [b,1], Yuan Jiang [a], La Zhang [c], Jiao Guo [g], Haichuan Liu [g], Bin Jiang [g], Shenglong Li [g,**], Qiling Peng [d,***], Ning Jiang [e,f,h,****], Jianwei Wang [a,*]

[a] Department of Immunology, School of Basic Medical Science, Chongqing Medical University, Chongqing, 400016, PR China
[b] Hunan University of Medicine General Hospital, Hunan, 418000, PR China
[c] Department of Hepatobiliary Surgery, The First Affiliated Hospital of Chongqing Medical University, Chongqing, 400016, PR China
[d] Bijie Municipal Health Bureau, Guizhou, 551700, PR China
[e] Department of Pathology, School of Basic Medical Science, Chongqing Medical University, Chongqing, 400016, PR China
[f] Molecular Medicine Diagnostic and Testing Center, Chongqing Medical University, Chongqing, 400016, PR China
[g] School of Basic Medical Science, Chongqing Medical University, Chongqing, 400016, PR China
[h] Department of Pathology, The First Affiliated Hospital of Chongqing Medical University, Chongqing, 400016, PR China

ARTICLE INFO

Keywords:
Immune checkpoint inhibitors
Aggregation-induced emission
Photodynamic therapies
Immunogenic cell death
Malignant melanoma

ABSTRACT

Immune checkpoint inhibitors (ICIs) become integral in clinical practice, yet their application in cancer therapy is constrained by low overall response rates and the primary resistance of cancers to ICIs. Herein, this study proposes aggregation-induced emission (AIE)-based nanoparticles (NPs) for a more effective and synergistic approach combining immunotherapy and photodynamic therapy (PDT) to achieve higher responses than anti-PD-L1 monotherapy. The TBP@aPD-L1 NPs are constructed by functionalizing azide group-modified TBP-2 (TBP-N_3) with anti-PD-L1 antibodies via the DBCO-S-S-PEG_{2000}-COOH linker. The anti-PD-L1 target the tumor cells and promote the TBP-N_3 accumulation in tumors for enhanced PDT. Notably, the TBP-N_3, featuring aggregation-induced emission, boosts reactive oxygen species (ROS) generation through both type I and type II processes for enhanced PDT. The TBP@aPD-L1-mediated PDT induces more powerful effects of direct tumor cell-killing and further elicits effective immunogenic cell death (ICD), which exerts anti-tumor immunity by activating T cells for ICI treatment and reshapes the tumor immune microenvironment (TIME), thereby enhancing the efficacy of PD-L1 blockade of anti-PD-L1. Consequently, TBP@aPD-L1 NPs demonstrated significantly enhanced inhibition of tumor growth in the mouse model of malignant melanoma (MM). Our NPs act as a facile and effective drug delivery platform for enhanced immunotherapy combined with enhanced PDT in treating MM.

1. Introduction

Malignant melanoma (MM), originating from skin melanocytes, exhibits an exceptionally high degree of malignancy and ranks third among the most common types of skin cancer [1]. It is the main cause of death for skin cancer, with the global incidence of melanoma projected to increase to nearly 510,000 new cases and 96,000 deaths in the next decade [2,3]. Moreover, MM represents the type of solid tumor with the highest number of mutations, possessing the ability to evade the immune system [4,5]. For patients in advanced stages, the combination of surgical intervention with radiotherapy or chemotherapy is often required; nevertheless, it leads to significant damage to the body [6,7]. In recent years, immunotherapy has stood out as a groundbreaking approach that has revolutionized MM treatment by demonstrating

* Corresponding author. Department of Immunology, School of Basic Medical Science, Chongqing Medical University, Chongqing, 400016, PR China.
** Corresponding author. School of Basic Medical Science, Chongqing Medical University, Chongqing, 400016, PR China.
*** Corresponding author. Bijie Municipal Health Bureau, Guizhou, 551700, PR China.
**** Corresponding author. Department of Pathology, School of Basic Medical Science, Chongqing Medical University, Chongqing, 400016, PR China.
E-mail addresses: lishenglong@cqmu.edu.cn (S. Li), pqlpzy@cqmu.edu.cn (Q. Peng), jiangning@cqmu.edu.cn (N. Jiang), jianweiwangcn@cqmu.edu.cn (J. Wang).
[1] These authors contributed equally to this work.

https://doi.org/10.1016/j.mtbio.2024.101387
Received 9 September 2024; Received in revised form 17 November 2024; Accepted 5 December 2024
Available online 6 December 2024

robust anti-tumor activities through the reinvigoration of the host immune system [8,9]. The PD-L1 small molecular weight inhibitors or PD-L1 antibodies are extensively developed for immunotherapy [10,11]. They bind to PD-L1 on tumor cells, disrupt the PD-1/PD-L1 pathway and thereby restore anti-tumor immunity [12,13]. Immune checkpoint inhibitors (ICIs) in immunotherapy have gained approval as treatments for advanced MM, with anti-PD-L1 antibodies (atezolizumab, durvalumab, and avelumab) being the most widely used [12,13]. Despite its widespread clinical use, monotherapy with ICIs has limited efficacy and primary resistance in 60%–70 % of melanoma patients, and the response rates, which are still far from satisfactory, severely hinder their further clinical applications [14–17]. The issue of sensitivities to ICIs in these patients needs to be urgently addressed.

The combination of photodynamic therapy (PDT) and ICI therapy demonstrates superior anti-tumor efficacy compared to ICI monotherapy. There is a growing interest in the use of PDT for combination therapy of cancers due to its low side effects, good spatiotemporal selectivity and no drug resistance [18–20]. More importantly, PDT effectively induces immunogenic cell death (ICD) of cancer cells, remodeling the tumor immune microenvironment (TIME), which transforms "cold" tumors into "hot" ones and activates anti-tumor immune responses [21–23]. Reprogramming the immunosuppressive TIME is highly beneficial for improving sensitivity to ICIs [24]. PDT utilizes photosensitizers (PSs) to absorb the light of the appropriate wavelength, interacting with molecular oxygen (O_2) to generate reactive oxygen species (ROS) which induces damage and death of cancer cells. PSs are key elements for PDT and their properties are crucial for the cytotoxic and immune effects induced by PDT. Conventional PSs are highly hydrophobic and prone to aggregation in biological systems. The aggregation-caused quenching (ACQ) effect greatly diminishes the efficacy of PDT [25]. The development of aggregation-induced emission luminogen (AIEgen) has brought a feasible solution to this issue and provided new opportunities for PDT. AIEgens exhibit significantly enhanced emissivity and ROS generation when aggregated, compared to when they are present as monomers, thereby compensating for the shortcomings of traditional PSs [26,27]. Moreover, the majority of currently developed PSs belong to type II, which are oxygen-dependent and their application is severely limited in hypoxic tumor environments. In contrast, type I PSs can effectively kill tumor cells even under hypoxic conditions, highlighting the urgent need for designing effective type I PSs for PDT in cancer treatment [28]. TBP-2, a novel AIEgen, efficiently generates ROS via both type I and type II processes, making it suitable for the construction of various anti-bacterial and anti-tumor systems. However, the high electronegativity and lack of targeting capabilities towards tumors limit its application [29]. Functionalizing TBP-2 with anti-PD-L1 not only improves the targeting of PSs to tumors but also enhances the effect of anti-PD-L1 by remodeling the TIME.

In this study, we reported the design of core-shell nanoparticles (NPs), TBP@aPD-L1 NPs, with the core of TBP-2 functionalized by anti-PD-L1 via the DBCO-S-S-PEG_{2000}-COOH linker. We initially modified TBP-2 with an azide group (-N_3) to generate TBP-N_3, allowing the -N_3 of TBP-N_3 to conjugate to the linker through a click chemistry reaction. Subsequently, amphipathic TBP-linkers self-assembled into nanoparticles, exposing carboxyl groups (-COOH) on the surface to react with amino groups (-NH_2) of anti-PD-L1 by amidation reaction to obtain TBP@aPD-L1 NPs. TBP-2 effectively avoided the disadvantages of ACQ for enhanced PDT due to its AIE properties and significantly enhanced ICD induction in tumor cells, thus further synergistically promoting the immunotherapeutic effect of anti-PD-L1. TBP@aPD-L1 NPs were precisely delivered to the tumor cells because of the tumor-targeting effects of anti-PD-L1, thereby achieving enhanced PDT effects as well. We demonstrated that TBP@aPD-L1 NPs were much more effective in inhibiting tumor growth compared to anti-PD-L1 alone or TBP-N_3 mediated PDT. This "all in one" nanoplatform effectively modulated the TIME by DC maturation and T cell infiltration and combated MM through the enhanced synergistic effects of PDT and immunotherapy (Scheme 1). This strategy offers a promising approach for designing nanomedicine using AIEgens, while also expediting the clinical application of AIEgens as PSs. The combination of AIEgens and ICIs introduces novel possibilities for enhancing immunotherapy, developing multimodal synergistic treatments and providing a promising therapeutic option for patient populations exhibiting limited responses to ICIs.

2. Experimental section

2.1. Chemicals and reagents

TBP-N_3 was provided by the laboratory of Professor Wenjun Miao (Chongqing, China). DBCO-S-S-PEG_{2000}-COOH was acquired from Chongqing Yusi Medical Technology Cable Co., Ltd (Chongqing, China). Anti-PD-L1 antibodies (BE0101) were purchased from BioXCell (New Hampshire, USA). Dimethyl sulfoxide (DMSO) was provided by Kelong Chemical Co., Ltd (Chengdu, China). 1-Ethyl-(3-dimethylaminopropyl) carbodiimide hydrochloride (EDC), N-Hydroxy succinimide (NHS) and 9,10-Anthracenediyl-bis(methylene)-dimalonic acid (ABDA) were obtained from Macklin (Shanghai, China). Roswell Park Memorial Institute (RPMI)-1640 Medium and 0.25 % Trypsin-ethylenediaminetetraacetic acid (EDTA) were obtained from Gibco Life Technologies (Grand Island, USA). Fetal Bovine Serum (FBS) was purchased from VivaCell (Shanghai, China). The murine melanoma cell line (B16F10) was from Procell Life Science & Technology (Hubei, China). The murine pulmonary epithelial cell line (MLE-12) was obtained from WheLab (Shanghai, China). Cell counting kit-8 (CCK-8) was obtained from TargetMol (Boston, USA). 2,7-Dichlorodihydrofluorescein diacetate (DCFH-DA) and YO-PRO-1 were from Beyotime Biotechnology (Shanghai, China). Singlet oxygen sensor green (SOSG) was acquired from MeilunBio (Dalian, China). Anti-calreticulin (27298-1-AP) and GAPDH mouse antibodies (60004-1-Ig) were from Proteintech (Wuhan, China). APC-CD80 monoclonal antibodies (17-0801-81) were from Thermo Fisher Scientific (Waltham, USA). All other chemicals were of analytical grade and did not require further purification. All experiments were conducted with Deionized (DI) water (Millipore, USA, 18.2 MΩ).

2.2. Synthesis and characterization of TBP@aPD-L1 nanoparticles

TBP-N_3 (1 mg) and DBCO-S-S-PEG_{2000}-COOH linker (2 mg) were dissolved and mixed in DMSO solution, then the mixture slowly added to DI water (9500 μL) and treated with ultrasound for 1 min. The TBP-S-S-PEG_{2000}-COOH (TBP-linker) self-assembled to form nanoparticles (NPs) after stirring at 300 rpm overnight at room temperature. Next, the TBP-linker mixtures were dialyzed using dialysis sacks of MWCO 5000Da and stored at 4 °C. The suspensions of TBP-linker NPs (2 mL) were diluted to 8 mL with DI water and subsequently reacted with anti-PD-L1 (100 μg) at 25 °C for 4 h in the presence of NHS (17.4 μg) and EDC (15.3 μg). After dialysis with the dialysis bag of 300 kDa, TBP@aPD-L1 NPs were collected and stored at 4 °C. Then the TBP-N_3, TBP-linker NPs, and TBP@aPD-L1 NPs were characterized by transmission electron microscopy (TEM, JEM-2100F, JEOL Ltd., Japan). Zeta potentials (ζ) using Malvern Zetasizer (Nano ZS90, UK). We used a UV–vis spectrometer (Techcomp UV-2600, China) to quantify the TBP@aPD-L1 NPs. Fluorescence signals of TBP-N_3 were measured by a spectrofluorometer FS5 (Edinburgh Instruments, UK).

2.3. The assay of intracellular GSH content

B16F10 cells were seeded in six-well plates at a density of 1×10^5 cells per well and cultured overnight. B16F10 cells were co-incubated with nanoparticles for 6 h, after the cell density reached 80 %. Then, the cells were rinsed twice with 1 mL of PBS and collected by centrifugation at 1000 rpm for 5 min. The cell pellet was sonicated using the Ultrasonic Cell Disruptor (Power: 300 W) in an ice-water bath. The

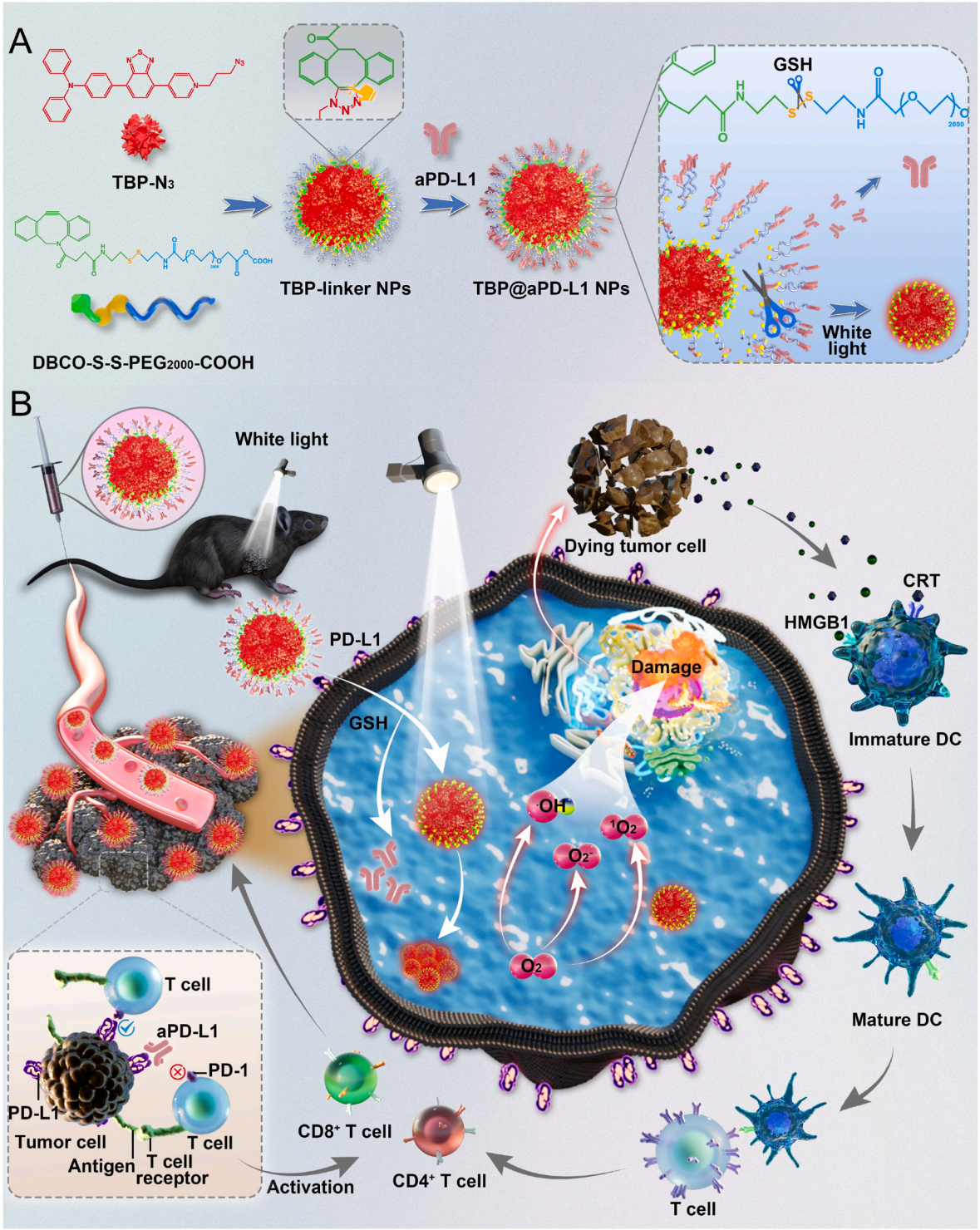

Scheme 1. Schematic illustration of AIEgen-self-assembled NPs with anti-PD-L1 functionalization for enhanced synergistic PDT and immunotherapy against MM. **(A)** Schematic illustration of TBP@aPD-L1 NPs synthesis. **(B)** Schematic illustration of robust systemic anti-tumor immunity activated by TBP@aPD-L1 NPs through a combination of PDT to trigger ICD and PD-L1 blockade. The B16F10 model was constructed using C57BL/6J mice, and TBP@aPD-L1 NPs were injected via the tail vein. NPs targeted tumor cells via anti-PD-L1 and released anti-PD-L1 in the presence of glutathione (GSH), which exerted PD-L1 blockade for ICI treatment. TBP@aPD-L1 NPs generated ROS via I and II pathways under white light irradiation, leading to tumor cell destruction and triggering effective ICD, which further remodels the TIME by inducing DCs maturation and T cells infiltration and transforms immunologically "cold" tumors into "hot" tumors, improving the efficacy of PD-L1 blockade. This "all in one" nanoplatform effectively enhanced PDT and immune responses and combats MM through the synergistic effects of PDT and immunotherapy.

ultrasonication lasts for 5 s at 30 s intervals, and the process is repeated 5 times. At the end of the treatment, the sample was centrifuged at 4 °C, 12000 rpm for 15 min, and the supernatant was collected. The supernatant was assayed using a GSH detection kit.

2.4. Studies of ROS generation in vitro

The ABDA solution (80 μM) was mixed with TBP-N_3 (10 μM), TBP@aPD-L1 (10 μM), and Chlorin e6 (Ce6, 10 μM), respectively, in water (2 mL) under dark conditions, and then the mixtures were irradiated (0.1 W cm^{-2}, 5 s each time). The ABDA solution (80 μM) was mixed with TBP-N_3 (10 μM), TBP@aPD-L1 (10 μM), and Rose Bengal (RB, 10 μM), respectively, in water (2 mL) under dark conditions, and then the mixtures were irradiated (0.1 W cm^{-2}, 5 s each time). The absorption of ABDA at 378 nm was recorded to obtain the singlet oxygen ($^1O_2$) formation rate. For the detection of hydroxyl radical (•OH), the different nanoparticles and 3,3′,5,5′-Tetramethylbenzidine (TMB) were mixed and irradiated, and the change in absorbance of TMB at 650 nm was measured on a UV–Vis spectrometer. 5,5-dimethyl-1-pyrroline-N-oxide (DMPO, 70.8 mM) was mixed with TBP@aPD-L1 NPs (1 mM) and irradiated by white light (0.1 W cm^{-2}, 5 min). The signals of •OH were recorded by an ESR spectrometer (Bruker EMXplus-6/1, Germany).

2.5. Anti-PD-L1 release assay of TBP@aPD-L1 NPs

TBP@aPD-L1 NPs (10 μM) were mixed with glutathione (GSH, 10 mM) and subsequently dialyzed in PBS. The absorbances of anti-PD-L1 in the dialysate at 280 nm at different time points were measured by UV–vis spectroscopy.

2.6. Cell culture and cytotoxicity assay

The bone marrow (BM) cells were collected from the bone marrow of 8-week-old C57BL/6J mice and stimulated with granulocyte-macrophage colony-stimulating factor (GM-CSF, 20 ng mL^{-1}) and interleukin 4 (IL-4, 10 ng mL^{-1}) to generate BM-derived dendritic cells (BMDCs). In short, after removing all muscle tissues from the femurs and tibiae, the bones were placed in a 10 cm dish with RPMI-1640. Both ends of the bones were cut with scissors in the dish, and then the marrow was flushed out using RPMI-1640 (2 mL) with a syringe. The cell suspension was passed through nylon mesh to remove small pieces of bone and debris, and red cells were lysed with ammonium chloride. After washing, 2×10^5 cells were resuspended in the medium supplemented with GM-CSF and IL-4 and then placed in Petri dishes. On day 3, an equal volume of fresh medium supplemented with GM-CSF and IL-4 was added to the plate. On day 6, 50 % of the medium was aspirated and replaced with equal volume of fresh medium containing GM-CSF and IL-4. Dendritic cells (DCs) were harvested on day 7 of culture based on the morphological accumulation of medium-sized 10-cell to 50-cell DC aggregates, which appear at this time loosely attached to adherent cells [30,31]. B16F10 cells were cultured at 37 °C in an incubator containing 5 % CO_2 and cultured in RPMI-1640 medium containing 10 % FBS and 1 % Penicillin-Streptomycin Solution. B16F10 cells were seeded into 96-well plates with 6×10^3 cells/well and cultured overnight. Then, the cells were incubated with different concentrations of TBP-N_3 and TBP@aPD-L1 NPs for 12 h before being irradiated by white light. After incubation for another 12 h, the cytotoxicity was evaluated by CCK-8 assay according to the manufacturer's instructions.

2.7. Western blot

Total protein: Cells were washed with pre-cooled PBS and lysed with Cell Lysis Buffer (200 μL) for Western and IP containing 1 % protease inhibitors (Phenylmethanesulfonyl fluoride, PMSF, Beyotime Biotechnology) for 30 min at 4 °C. Then supernatants were harvested after centrifugation at the speed of 12000 rpm for 15 min.

Membrane protein: The washed cells were collected in EP tubes, and 1 mL of Membrane Protein Extraction Reagent A was added. After gentle mixing, the tubes were placed on ice for 15 min to facilitate the release of cell membrane proteins. The cell suspension was then transferred to a pre-cooled glass homogenizer and subjected to approximately 30 homogenization cycles to ensure adequate cell disruption. After homogenization, the suspension was centrifuged at 700 g for 10 min at 4 °C to collect the supernatant. The supernatant was then centrifuged again at 14,000 g for 30 min to precipitate membrane fragments. After aspirating the supernatant, 200 μL of Membrane Protein Extraction Reagent B was added. The precipitate was resuspended by vortexing for 5 s, then incubated on ice for 5 min. This step was repeated twice to ensure complete extraction of membrane proteins. Finally, the supernatant was collected and centrifuged at 14,000 g for 5 min to obtain a purified membrane protein solution.

The protein solution was mixed with 5 × SDS-PAGE sample loading buffer and denatured at 100 °C for 10 min. Equal amounts of the proteins were resolved by 7.5 % SDS-PAGE gels and transferred to the polyvinylidene fluoride (PVDF) membrane. Membranes were blocked with 5 % skim milk in TBST buffer and incubated overnight at 4 °C with primary antibodies (1:1000 dilution) in TBST. Then the membrane was incubated with horseradish peroxidase (HRP) conjugated goat anti-mouse or goat anti-rabbit secondary antibody (1:1000 dilution) in TBST buffer at room temperature with shaking for 60 min. Finally, protein expression levels were detected by chemiluminescence (ECL) reagent and the images were captured using CheniDoc Imaging System (Thermo Scientific Waltham).

2.8. Immunofluorescence staining

Experimental procedure for immunofluorescence staining of cell cultures. B16F10 cells after treatments of different nanoparticles were fixed with 4 % paraformaldehyde for 15 min and then blocked by 5 % BSA for 1 h. Then B16F10 cells were incubated with specific primary antibodies for 30 min at 4 °C and followed by incubation with fluorescent dyes-labeled secondary antibodies at room temperature for 1 h. Immunofluorescence staining was imaged using a Leica TCS SP8 confocal laser scanning microscope (CLSM). Besides, intracellular ROS levels were detected with DCFH-DA and SOSG.

Experimental procedure for immunofluorescence staining of tissue. Fix the tissue sample using paraformaldehyde embed it in paraffin, and cut it into thin sections (8 μm thick) using a microtome. Perform antigen retrieval by boiling tissue sections in a citrate buffer (pH 6.0) for 15 min in a microwave. Block non-specific binding sites by incubating tissue sections in 5 % BSA for 1 h at room temperature. Incubate the tissue sections with primary antibodies (diluted in blocking buffer) overnight at 4 °C, and then wash the tissue sections with PBS (3 times, 5 min each) to remove the unbound primary antibody. Incubate the tissue sections with the secondary antibody (1:200 dilution) in blocking buffer for 1 h at room temperature, and then wash the tissue sections with PBS (3 times, 5 min each) to remove unbound secondary antibodies. Stain the nuclei with a nuclear counterstain (DAPI) diluted in PBS for 10 min at room temperature. Next, mount tissue sections onto glass slides using the antifade mounting medium (Beyotime) and cover with a coverslip. Visualize immunofluorescence signals using CLSM.

2.9. Detection of $^1O_2$ and H_2O_2 under hypoxic conditions in vitro

To construct the hypoxic tumor model, B16F10 cells were cultured in an incubator chamber at 37 °C in a humidified, 1 % O_2, 5 % CO_2, and 95 % N_2 atmosphere for 0 h, 6 h and 12 h. The HIF-1α expression levels in different treatment groups were detected by western blot. To detect the $^1O_2$, B16F10 cells were incubated with SOSG (50 μM) for 4 h after different times of hypoxia. The fluorescence was immediately observed by CLSM after being washed with PBS two times. To detect the ROS via type I processes ROS via I, the B16F10 cells were treated with PBS, anti-

PD-L1, TBP-N_3, and TBP@aPD-L1 (2 μg mL^{-1}), respectively, and then cultured under hypoxia condition for 12 h. The cells were incubated with dihydrorhodamine 123 (DHR123, 10 μM) for 30 min under normoxic or hypoxic conditions. After then washed with PBS for two times, the cells were irradiated with white light (0.1 W cm^{-2}, 6 min). The fluorescence was immediately observed using CLSM.

2.10. Induction of DCs maturation

B16F10 cells were seeded in the upper chamber at a density of 1 × 10^6 cells per well and cultured overnight. B16F10 cells were incubated with the different nanoparticles for 6 h and irradiated with white light (0.1 W cm^{-2}, 6 min). The upper B16F10 cells were then co-cultured with the lower DCs. After 24 h of co-incubated, DCs were collected for flow cytometry (FCM) assays. Meanwhile, the lower supernatants were collected to detect tumor necrosis factor-α (TNF-α) expression by an enzyme-linked immunosorbent assay (ELISA) kit. The ELISA was performed according to the protocol of Quanzhou Jiubang Biotechnology Co., Ltd.

2.11. Flow cytometry

To detect TBP@aPD-L1 NPs targeted B16F10 cells, 6-well plates with B16F10 cell densities reaching 80 % were collected after incubation with nanoparticles for 1, 2, and 4 h. The B16F10 cells were then directly detected of red fluorescence through the PercP-Cy5.5 channel. For apoptosis detection in B16F10 cells, B16F10 cells were treated with different nanoparticles for 12 h after reaching 80 % density in 6-well plates. The culture was continued for an additional 12 h after 6 min of light exposure per well. B16F10 cells were resuspended in FACS buffer (200 μL), and DAPI (0.5 mg mL^{-1}) and Annexin V-APC (2 μL) were added. Incubate at room temperature away from light for 15 min and then test. For the examination of DCs maturation stimulation, DCs were collected and incubated with CD16/CD32 antibody for 10 min. Then, the cells were labeled with APC-CD80 antibodies for 30 min at 4 °C. Afterward, the cells were rinsed twice with 1 mL of PBS and centrifuged at 300 g for 5 min. Ultimately, the cells were resuspended in FACS buffer (200 μL) for flow cytometry analysis (Becton, Dickinson (BD) and Company FACS Celesta, USA).

2.12. B16F10 mouse melanoma model

The male C57BL/6J mice at 6 weeks of age were obtained from the Experimental Animal Center of Chongqing Medical University (Chongqing, China). The mice were administered 1 × 10^6 B16F10 cells (100 μL of PBS for each mouse) in the right dorsal. When tumor volume reached about 80∼120 mm^3, the mice were randomly divided into six groups (n = 5): PBS (control), free anti-PD-L1, TBP-N_3, TBP@aPD-L1, TBP-N_3 with white light (TBP-N_3 + L), TBP@aPD-L1 with white light (TBP@aPD-L1 + L). The dosages of TBP-N_3 were 10 mg kg^{-1}. Treatments were administered on days 0, 3, and 7 via tail vein injections of nanoparticles, followed by tumor irradiation with white light (0.1 W cm^{-2}, 20 min) at 12 h post-injection. Body weight and tumor volume were monitored every two days. The tumor volume was calculated as the formula: tumor volume = $(\text{tumor width})^2/2 \times$ tumor length. The mice were sacrificed after 12 days. Subsequently, the tumors were collected and analyzed by Hematoxylin & Eosin (H&E) staining and immunofluorescence staining to estimate the anti-tumor efficacy. All animal experiments were performed according to the protocols approved by the Animal Care and Use Committee of Chongqing Medical University (Chongqing, China) (Approval number: IACUC-CQMU-2023-0304).

2.13. Fluorescent localization of TBP-N_3 in vivo

The mice were sacrificed to dissect the tumors at different time points after intravenous administration (10 mg kg^{-1}) of TBP-N_3 or TBP@aPD-L1 NPs. The tissue sample was immediately stored in an OCT embedding box and rapidly frozen using liquid nitrogen. Remove the tissue block and immediately place it in a cryostat for frozen sectioning, with a section thickness of 8 μm. Subsequently, the fluorescence intensity of each group of tumor tissues was observed by the CLSM.

2.14. The process of H&E staining

The tissue sections are deparaffinized in xylene and then rehydrated through a series of graded alcohols. The sections are stained with hematoxylin, which binds to the nuclei. The sections are then rinsed in water. The sections are differentiated in acid alcohol, which removes excess hematoxylin from the tissue. The sections are briefly rinsed in alkaline water to "blue" the nuclei, which enhances the contrast between the nuclei and the cytoplasm. The sections are counterstained with eosin, which stains the cytoplasm and extracellular matrix. The sections are then dehydrated through a series of graded alcohols and cleared in xylene before mounting with a coverslip.

2.15. Statistical analysis

GraphPad Prism software (vision 9.0.0 (121)) was applied for data analysis. The results were presented as mean ± SD of at least three independent experiments. Student's t-test was utilized to determine the statistical significance between the two groups. Three or more groups were compared by one-way analysis of variance (ANOVA). A p-value <0.05 was considered statistically significant (*$p < 0.05$, **$p < 0.01$, ***$p < 0.001$, ****$p < 0.0001$), ns: no significance.

3. Results and discussion

3.1. Preparation and characterization of TBP@aPD-L1 NPs

We selected TBP-2 as our PS to address the ACQ issue of PSs due to its excellent AIE properties in aqueous media and remarkable PDT effects in the hypoxic environment [32]. First of all, TBP-2 was modified by the -N_3 to form TBP-N_3 complexes (Scheme 1A). The -N_3 modification facilitated its conjugation to the DBCO-S-S-PEG_{2000}-COOH linker through click chemistry. The successful -N_3 modification on TBP-2 was confirmed by ^{1}H NMR and mass spectrum (Fig. S1 A-B).The PL intensity results showed that TBP-N_3 still retained good AIE characteristics, with fluorescence intensity increasing as the proportion of water in the solvent increased (Fig. 1A–B). TBP-N_3 exhibited the same absorption peak at 480 nm as TBP-2 and the emission peak at 725 nm occurring in the red spectral region (Fig. S2). All these results are consistent with the previous report on TBP-2 [32]. Additionally, -N_3 modification greatly improved the membrane permeability of TBP-2, and the red fluorescence of TBP-2 was intracellularly observed in the cytoplasm (Fig. S3). Although in previous studies, TBP-2 was proved to have a high ROS production yield, its photodynamic effects on mammalian cells are restricted by its two positive charges [33]. Due to the negative charge on the cell membrane, TBP-2 was adsorbed on the cell membrane, resulting in a low translocation ability into cell interiors and hindering its capacity to exert satisfactory PDT effects [34]. So delivery systems based on platelet membrane membranes and bacteria were developed to enable the effective intracellular accumulation of TBP-2 [33,35]. -N_3 modification significantly increased the cellular uptake of TBP-2, thereby laying the foundation for enhanced PDT efficacy. Subsequently, TBP-N_3 was employed to construct nanoparticles in the following experiments.

The synthetic procedures of TBP@aPD-L1 NPs were clearly illustrated (Scheme 1A). In the beginning, the linker was conjugated to TBP-N_3 to generate the amphiphilic TBP-linker NPs by the click chemistry reaction. Fourier-transform infrared (FT-IR) spectroscopy showed that the characteristic peaks of the -N_3 at 2100 cm^{-1} disappeared on the TBP-linker NPs, and the C=O bands peak at 1640 cm^{-1} as well as the C-O bands at 1100 cm^{-1} of the linker appeared on the TBP-linker NPs,

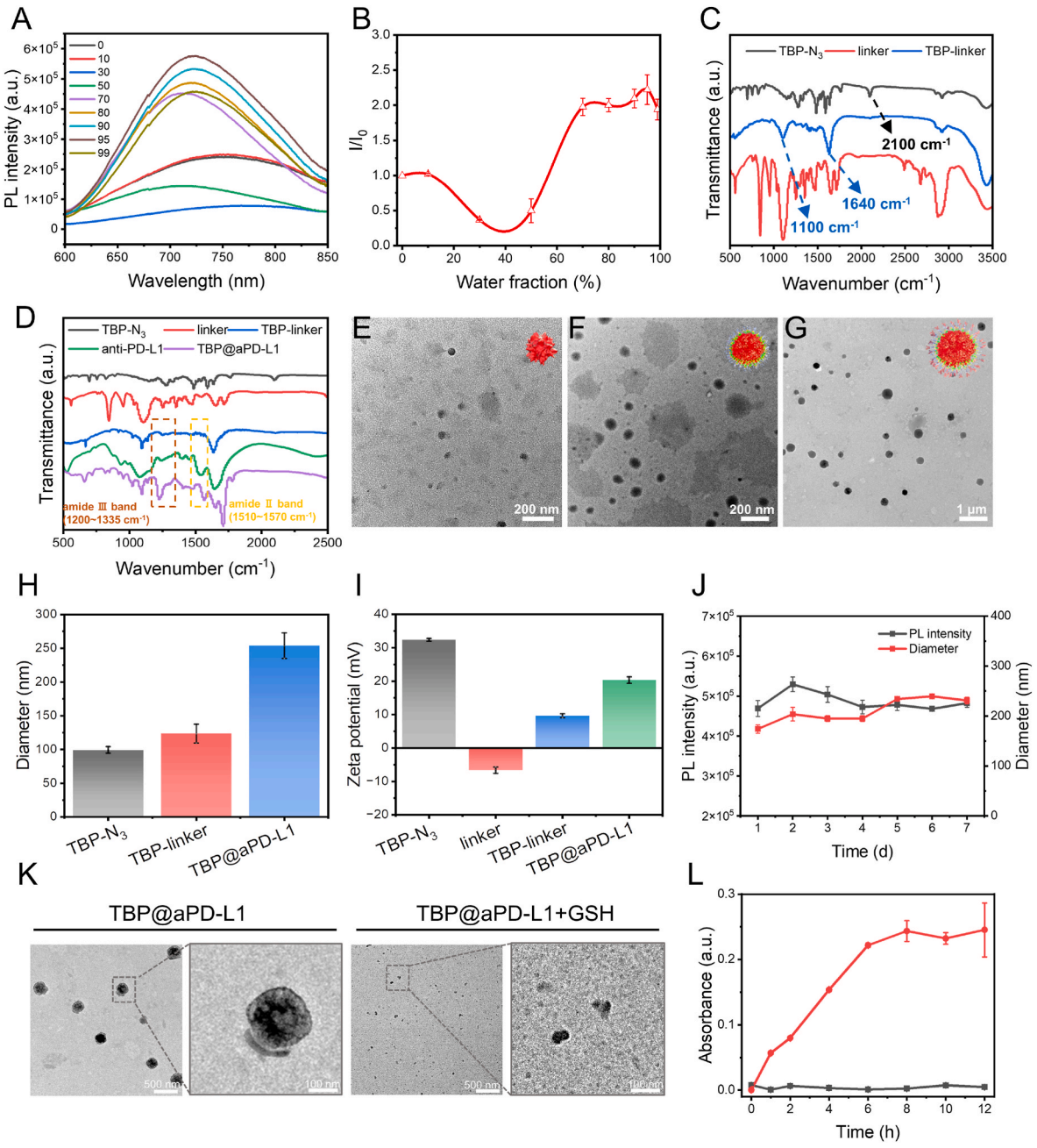

Fig. 1. Preparation and characterization of TBP@aPD-L1 NPs. **(A)** The PL intensity of 200 μM TBP-N_3 in DMSO/water mixtures with different water fractions (*f*w). Conditions: λ_{ex} = 488 nm. **(B)** The plots of PL intensity at 725 nm of TBP-N_3 at different *f*w. **(C)** FT-IR spectrum of TBP-N_3, linker, TBP-linker NPs. **(D)** FT-IR spectroscopy of TBP-N_3, linker, TBP-linker NPs, anti-PD-L1 and TBP@aPD-L1 NPs. **(E–G)** TEM images of TBP-N_3, TBP-linker NPs and TBP@aPD-L1 NPs. **(H)** Hydrodynamic size distribution of TBP-N_3, TBP-linker NPs and TBP@aPD-L1 NPs measured by DLS. **(I)** Zeta potential of different materials in PBS. **(J)** Fluorescence intensity and hydrodynamic size of TBP@aPD-L1 NPs dispersed in PBS for different storage periods. **(K)** TEM images of TBP@aPD-L1 NPs with or without GSH. **(L)** UV–vis absorption spectra of anti-PD-L1 released from TBP@aPD-L1 NPs at PBS buffer (Red: TBP@aPD-L1 NPs + GSH, Black: TBP@aPD-L1 NPs).

proving that the linker was successfully conjugated to TBP-N_3 (Fig. 1C) [36,37]. Anti-PD-L1 were further modified to the outside of the TBP-linker NPs through amide bonds between the -NH_2 on the antibodies and the -COOH on the linkers to form TBP@aPD-L1 NPs. We firstly employed Raman spectroscopy to confirm the conjugation of the antibody and linker. As shown in Fig. S4A, the Raman peaks of the dibenzocyclooctyne group (-DBCO) of the linker appear on the anti-PD-L1-linker at 2158 cm^{-1} as characteristic peaks, and at the same time the Raman peaks at 1000 cm^{-1} and 1670 cm^{-1} for phenylalanine and tryptophan in the anti-PD-L1 appear on the anti-PD-L1-linker, indicating the successful conjugation of the antibody and linker [38, 39]. The UV–vis absorption spectra demonstrate that TBP@aPD-L1 NPs exhibited typical TBP-2 peaks at 480 nm, and an obvious change in the shape of the spectra at 310 nm compared to TBP-linker NPs, suggesting the successful anti-PD-L1 conjugation to TBP-linker NPs (Fig. S4B). To further confirm the conjugation of the antibodies to TBP-linker NPs, the FT-IR analysis was conducted. Compared to the TBP-linker group, the spectroscopy demonstrated that TBP@aPD-L1 NPs exhibited the characteristic peaks of the antibody, including the amide II band at 1510~1570 cm^{-1} and the amide III band at 1200~1335 cm^{-1}, indicating the successful conjugation of the anti-PD-L1 to TBP-linker NPs (Fig. 1D). Subsequently, the optimal ratio of antibodies to the TBP-linker

NPs for the synthesis of TBP@aPD-L1 NPs was assessed. Different concentrations of anti-PD-L1 to 25 μg mL^{-1} TBP-linker NPs were used to generate TBP@aPD-L1 NPs. The intensity of red fluorescence on B16F10 cells stained by TBP@aPD-L1 NPs was examined via FCM, and the ratio of 10 μg mL^{-1} antibody to 25 μg mL^{-1} TBP-linker NPs was eventually determined with the highest fluorescence (Fig. S5A). The morphology and size of TBP-N_3, TBP-linker NPs and TBP@aPD-L1 NPs were examined by transmission electron microscope (TEM). TBP-N_3 formed small, irregular nanoparticles with diameters of tens of nanometers through aggregate formation (Fig. 1E). When exposed to DI water under ultrasound conditions, TBP-linkers self-assembled into NPs with a hydrophilic outer shell and a hydrophobic TBP-N_3 inner core. The TBP-linkers formed uniform NPs with larger diameters of around 100 nm (Fig. 1F). TBP@aPD-L1 NPs became further enlarged after antibody modification with diameters over 200 nm (Fig. 1G). Dynamic light scattering (DLS) also demonstrated that the particle size increased with modification, which was consistent with the TEM results (Fig. 1H). Zeta potentials of nanoparticles in different groups were measured. After TBP-N_3 was loaded with the linker, the potential decreased from +32.3 mV (TBP-N_3) to +9.63 mV (TBP-linker) due to the negative charge of the -COOH on the linker. It then increased to +20.3 mV (TBP@aPD-L1) after the conjugation of the anti-PD-L1 (Fig. 1I). All these results indicate the successful synthesis of TBP@aPD-L1 NPs. To investigate the stability of the TBP@aPD-L1 NPs, the newly synthesized NPs were dispersed in PBS for 7 days. The stability was evaluated by comparing the size and fluorescence with DLS and fluorescence spectrophotometry, respectively. Fig. 1J shows no significant changes in DLS and fluorescence intensity, indicating that TBP@aPD-L1 NPs exhibited good stability in PBS. To facilitate subsequent experiments, the concentration of TBP@aPD-L1 NPs was quantified by TBP-N_3 absorbance according to the calibration curve by the UV–vis absorbance of TBP-N_3 (Fig. S5B).

Tumor cells have the high content of glutathione (GSH), with concentrations as high as 10 mM [40]. As an important antioxidant, GSH scavenges ROS produced in the cell and impedes PDT action [41,42]. Therefore, the nanoplatform, which simultaneously generates ROS and consumes GSH, is ideal for PDT. While TBP@aPD-L1 NPs are exposed to GSH to release anti-PD-L1 and TBP-2, the disulfides in the linker could consume GSH in tumor cells. To confirm the responsiveness of TBP@aPD-L1 NPs to GSH, changes in particle size were detected by TEM and DLS after GSH treatment and the results showed that the particle size was significantly reduced after GSH treatment (Fig. 1K and Fig. S6). Meanwhile, the release of anti-PD-L1 was assayed by measuring the UV–vis absorbance of the dialysate at 280 nm at different time points during dialysis. The absorbance increased over time and reached the release plateau at 8 h after GSH treatment (Fig. 1L). Furthermore, to validate the GSH consumption by NPs, the cells were ultrasonically lysed after treatment and the concentration of GSH was detected using the GSH detection kit. GSH in the cell was found to be significantly reduced in the TBP-N_3 and TBP@aPD-L1 treated groups. And the level of GSH was significantly lower in the TBP@aPD-L1 group than that in the TBP-N_3 group. This indicates that TBP@aPD-L1 NPs could consume GSH, which is conducive to impairing the scavenging of ROS and weakening the antioxidant capacity of tumor cells (Fig. S7). Unexpectedly, the GSH level in the TBP-N_3 treated group was also reduced, indicating that TBP-N_3 itself acts as a GSH scavenger. This might be due to multiple unsaturated bonds in TBP-N_3. Unsaturated bonds serve as reaction sites to GSH for irreversible Michael addition by GSH, resulting in GSH consumption [43,44]. All these data demonstrated the GSH-responsive TBP@aPD-L1 NPs were successfully synthesized.

3.2. ROS generation by TBP@aPD-L1 NPs via both type I and type II pathways

ROS production is the major mechanism by which PDT triggers tumor cell death. Due to the hydrophobicity of traditional PSs, their aggregation in physiological circumstances severely impairs ROS generation. The most noteworthy advantage of AIEgens is their excellent ROS generation ability in the aqueous environment [45]. To compare the ROS generation capacity with conventional and commercial PSs, we dissolved Chlorin e6 (Ce6), Rose Bengal (RB), TBP-N_3 and TBP@aPD-L1 NPs in water and then assayed their reactive singlet oxygen ($^1O_2$) production by the decomposition of ABDA upon white light irradiation. The absorbance of ABDA at 378 nm was recorded at various irradiation times (Figs. S8A–B). The decrease in absorbance of ABDA (ΔAbs) was utilized to evaluate the photosensitivity in ROS production. The absorbance decreased remarkably in the TBP-N_3 and TBP@aPD-L1 groups, which was much lower than that in the Ce6 and RB groups (Fig. 2A–B). Considering their superior performance than Ce6 and RB under the same circumstances, TBP-N_3 and TBP@aPD-L1 NPs show great potential as replacements for commercial PSs after further investigation into their biosafety. Subsequently, we examined the generation of total ROS in the cells after NPs treatment by FCM using the DCFH-DA probe. Fluorescence intensities in the control with PBS, anti-PD-L1, TBP-N_3 and TBP@aPD-L1 groups with no irradiation were low and comparable. The intensities of the DCFH-DA probe increased greatly in the TBP-N_3 and TBP@aPD-L1 groups after white light irradiation (TBP-N_3 + L and TBP@aPD-L1 + L, respectively), which indicates their robust ROS production for PDT (Fig. 2C and Fig. S8C). Immunofluorescence using the DCFH-DA probe verified that the ROS levels in the TBP-N_3 + L and TBP@aPD-L1 + L groups, especially in the TBP@aPD-L1 + L group, were significantly higher than those in the TBP-N_3 and TBP@aPD-L1 groups, respectively (Figs. S8D–E). Furthermore, the intracellular ROS generation of TBP-N_3 was further confirmed using a singlet oxygen sensor green (SOSG) probe. The stronger SOSG fluorescence intensity was exhibited in the TBP-N_3 + L and TBP@aPD-L1 + L groups, especially in the TBP@aPD-L1 + L group (Fig. 2D–E). Anti-PD-L1 modification could effectively promote the ROS production efficiency of TBP-N_3 in the cell, and this might be because the targeting ability of anti-PD-L1 enhances the accumulation of TBP-N_3 in cells. In the next section, the tumor-targeting of TBP@aPD-L1 NPs was further validated.

Most of the current PSs used in clinical settings work for PDT via the type II mechanism. The tumor microenvironment is hypoxic, so the application of traditional PSs is greatly restricted by the low O_2 concentration [46,47]. The effectiveness of PDT can be improved by the introduction of agents such as MnO_2 that elevate the O_2 concentration in the tumor microenvironment, which is referred to as oxygen-boosted PDT [48]. However, while MnO_2 catalyzes oxygen production in the tumor microenvironment, its efficacy may be hampered by the low concentration of the intracellular substrate (H_2O_2 < 50 μM) and biological toxicity [49]. ROS production is less oxygen-dependent in type I pathway and oxygen-dependent in type II pathway [50,51]. Therefore, it is urgently needed to develop less oxygen-dependent type I PSs for PDT treatment of cancers. In our study, we evaluated the ability of TBP@aPD-L1 to generate ROS through the type I pathway by measuring the •OH content. Firstly, we examined •OH by electron spin resonance (ESR) with DMPO as the spin-trap agent. With crystalline violet (CV) as the positive control, a typical ESR spectrum of DMPO-OH adduct derived from •OH was observed in the TBP-N_3 and TBP@aPD-L1 NPs groups upon white light irradiation (Fig. 2F). Next, 3,3′,5,5′-tetramethylbenzidine (TMB) was used to monitor the production of •OH, as TMB can be oxidized by •OH to the blue-green color with maximum absorbance at 650 nm. We observed the appearance of an absorption peak at 650 nm (Fig. 2G) and the color change of the solution (Fig. 2H) in the TBP-N_3 and TBP@aPD-L1 groups with TMB after white light irradiation. These results indicate that our NPs can effectively produce ROS via type I reaction, which greatly reduces the dependence on oxygen and achieves more efficient PDT in the tumor microenvironment. To confirm the type I ROS production in the cells, we established the cell culture models of hypoxia and assayed the ROS levels after different treatments in the hypoxic condition using dihydrorhodamine 123 (DHR123) probes. The expression of HIF-1α in B16F10 cells significantly increased after 6 h of hypoxia and became more pronounced after 12 h,

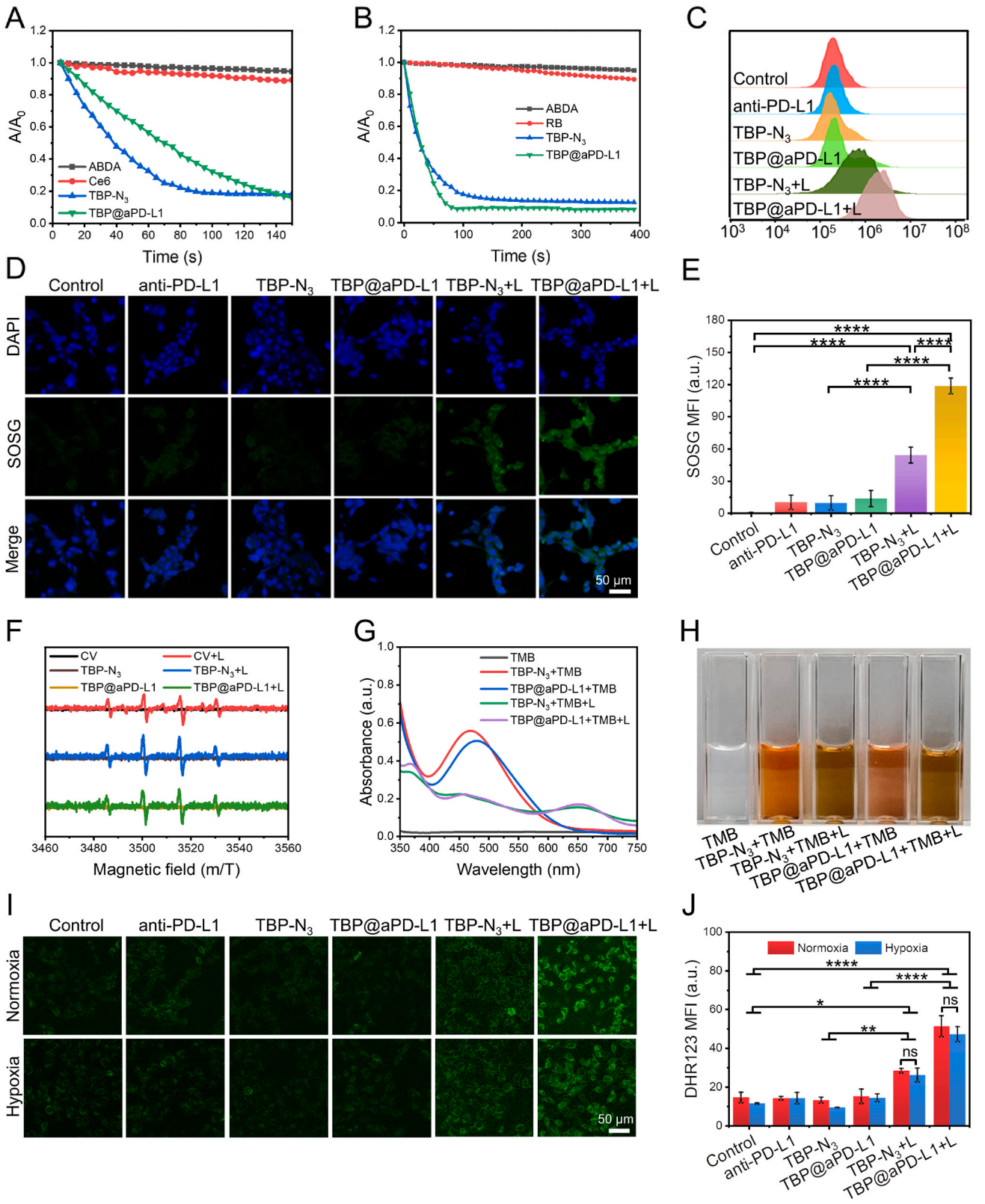

Fig. 2. ROS generation of NPs under light irradiation. **(A–B)** The detection of the $^1O_2$ generation by the degrading of ABDA indicator in the presence of Ce6, RB, TBP-N_3 and TBP@aPD-L1 NPs under white light irradiation. **(C)** Flow cytometry of B16F10 cells with ROS-reactive DCFH-DA to assess the ROS level. **(D–E)** The CLSM images and fluorescence intensity of SOSG were used to analyze the production of ROS in B16F10 cells after different treatments under white light irradiation. **(F)** ESR signals of DMPO in the presence of NPs before and after irradiation with white light. **(G–H)** Absorbance variations and color change of TMB at 650 nm after white light irradiation. **(I–J)** CLSM images and fluorescence intensity of DHR123 in B16F10 cells were analyzed to assess the effects of different treatments under normoxic and hypoxic conditions. "+ L" represents in combination with white light irradiation. Power density: 0.1 W cm^{-2}. Scale bars: 50 μm. The data shows the mean ± SD. (n = 3). Statistical significance was calculated by one-way ANOVA: $^*P < 0.05$, $^{**}P < 0.01$, $^{****}P < 0.0001$, ns: no significance.

which indicates that our cell culture model of hypoxia was successfully established (Figs. S9A–B). We then evaluated the $^1O_2$ level in B16F10 cells after hypoxia at distinct time points using SOSG probes. As shown in Figs. S9C–D, the fluorescence intensity of the SOSG probe showed a significant decrease after 12 h of hypoxia, compared to that in the normoxic group. This is consistent with the concept that the production of type II ROS is oxygen-dependent. B16F10 cells were then exposed to different treatments after 12 h of hypoxia and stained with DHR123 probes. The CLSM results show that the DHR123 fluorescence intensities in the TBP-N_3 + L and TBP@aPD-L1 + L groups were much higher than those in the groups without light irradiation, which suggests that TBP-N_3 could produce type I ROS. Additionally, the greater fluorescence intensity observed in the TBP@aPD-L1 + L group compared to the TBP-N_3 + L group provides evidence for the targeting capability of anti-PD-L1. More notably, the DHR123 fluorescence intensities remained comparable under hypoxic conditions to those under normoxic conditions, which indicates that the ROS production by TBP-N_3 could be less oxygen-dependent (Fig. 2I–J). All the data above indicate that TBP-N_3 and TBP@aPD-L1 NPs possess excellent capability to generate ROS through both type II and type I pathways.

3.3. *Targeting and enhanced photocytotoxic effects of TBP@aPD-L1 NPs in vitro*

All the current PSs used in PDT lack the ability to target tumor cells. Therefore, the precise and active targeting of PSs is achieved by coupling

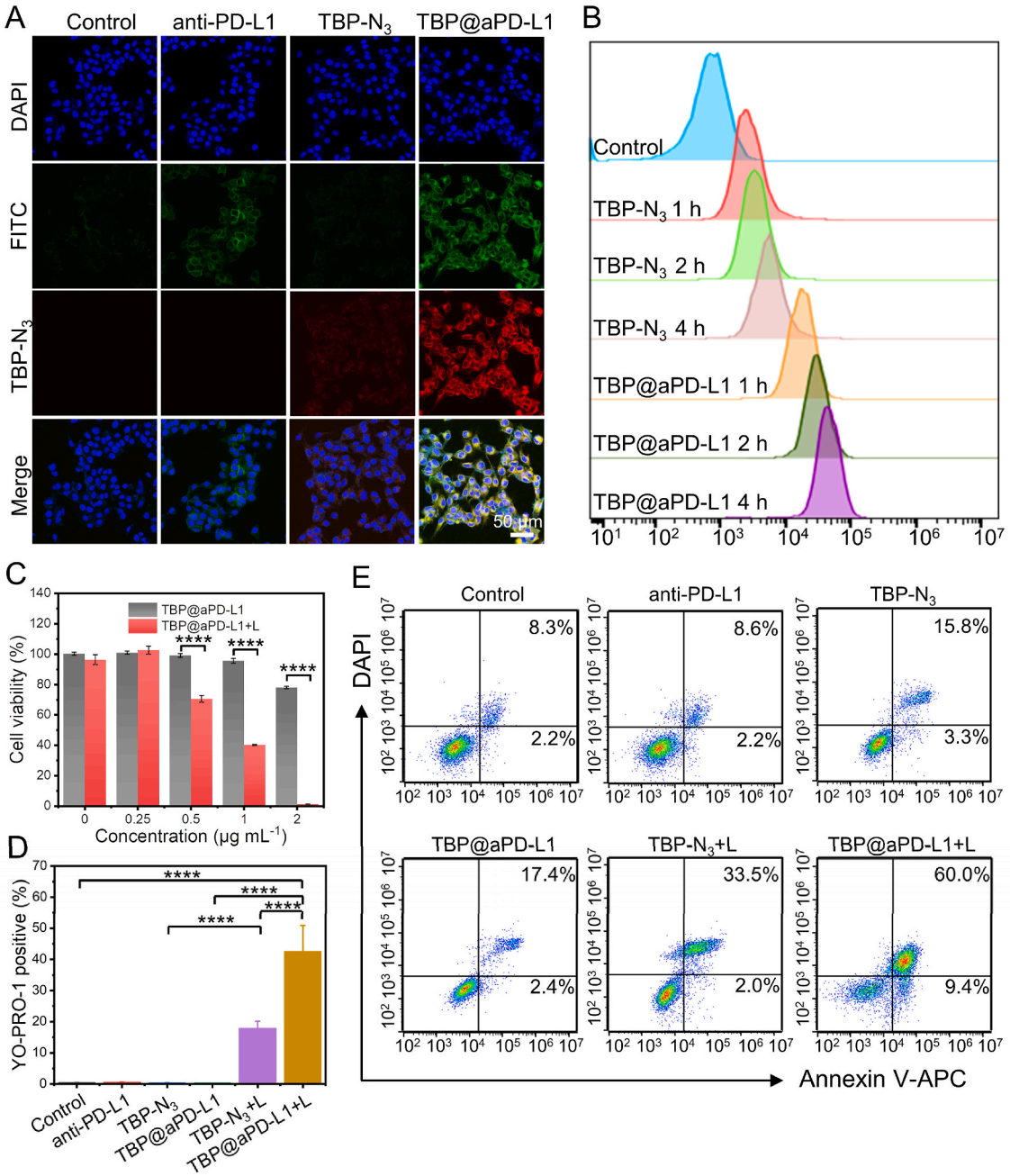

Fig. 3. Evaluation of the targeting ability and cell cytotoxicity for TBP@aPD-L1 NPs. **(A)** CLSM images of NPs specifically targeting B16F10 cells (Blue: DAPI-stained nuclei, Green: anti-PD-L1, Red: TBP-N_3). **(B)** The fluorescence of TBP-N_3 in B16F10 was assessed using flow cytometry after NPs treatments at different time points. **(C)** Cell viability of B16F10 cells incubated with different concentrations of TBP@aPD-L1 NPs for 24 h. **(D)** The percentage ratio of dead cells with different treatments. **(E)** Flow cytometry analysis of apoptosis in B16F10 cells after different treatments. "+ L" represents in combination with white light irradiation. Power density: 0.1 W cm^{-2}. Scale bars: 50 μm. The data shows the mean ± SD. (n = 3). Statistical significance was calculated by one-way ANOVA: ****$P < 0.0001$.

antibodies in the third generation of PSs [52,53]. In this study, we chose anti-PD-L1 for coupling TBP-2. As one of the most widely used ICIs in the clinic, anti-PD-L1 not only target the tumor with PD-L1 expression to achieve the precise delivery and accumulation of PSs into the tumor site, but also block the PD-1/PD-L1 signaling pathway to activate the immune cells. The combination of TBP-2 and anti-PD-L1 has not been studied yet. To validate the tumor cell-targeting and photocytotoxic effects of TBP@aPD-L1 NPs on tumor cells, B16F10 cells were applied for *in vitro* assay. According to both previous reports and our results, B16F10 highly expresses PD-L1, making it a suitable cell model for the TBP@aPD-L1 targeting study, with the mouse lung epithelium cell line MLE-12 as the control (Figs. S10A–B) [54,55].

B16F10 cells were incubated with anti-PD-L1, TBP-N_3 and TBP@aPD-L1 NPs. By immunofluorescence, the green fluorescence signals for the anti-PD-L1 could be clearly detected in the TBP@aPD-L1 and anti-PD-L1 groups. This suggests that TBP@aPD-L1 NPs exhibit the excellent ability to target tumor cells, similar to anti-PD-L1. We next detected the red fluorescence of TBP-N_3 excited by the 488 nm laser. No red fluorescence was detected in the control and anti-PD-L1 groups, whereas distinct red fluorescence was readily discernible in both the TBP-N_3 and TBP@aPD-L1 groups. The red fluorescence intensity of the TBP@aPD-L1 group was much greater than that of the TBP-N_3 group, which demonstrates that anti-PD-L1 functionalization endowed NPs with the capacity to target B16F10 cells and promoted the accumulation of NPs in B16F10 cells (Fig. 3A). In addition, these results further proved that the anti-PD-L1 was successfully coupled with TBP-linker NPs. We obtained the consistent results via FCM, confirming that the red fluorescence in B16F10 after the TBP@aPD-L1 treatment markedly exceeded that in the TBP-N_3 treated group. The modification with anti-PD-L1 significantly increased the fluorescence intensity of TBP-N_3 in the cells, and this increasing effect was time-dependent (Fig. 3B). In the phototherapeutic process, poor photostability of PSs upon light exposure severely limits the clinical application of PDT [56,57]. The photostability of TBP@aPD-L1 NPs was investigated by cellular imaging of B16F10 cells under continuous laser irradiation. After 120 scans with the 488 nm laser by CLSM, the red fluorescence signal of TBP@aPD-L1 NPs showed almost no attenuation, indicating our NPs had good photostability (Fig. S11). In particular, anti-PD-L1 induced up to 40 % of PD-L1 internalization after 2 h treatment (Figs. S12A–B). Anti-PD-L1 mediated efficient internalization enhances the endocytosis of NPs [58]. Effective targeting as well as efficient endocytosis can greatly promote the accumulation of PSs in tumor cells and enhance the therapeutic effect of PDT [59]. The usage of high doses of PSs can be avoided with our NPs by delivering the PSs precisely to specific tumor cell compartments while minimizing contact with normal cells. Therefore, our strategy of anti-PD-L1 modification on PSs effectively addresses the limitations of poor tumor targeting associated with traditional PSs, in contrast to PD-L1 regulation strategies that downregulate PD-L1 expression to block the PD-L1/PD-1 signaling pathway [60,61].

Next, we validated the photocytotoxic effects of TBP@aPD-L1 NPs by CCK-8 kit under white light irradiation. To assess the dark toxicity of TBP-N_3, varying concentrations of TBP-N_3 were added to B16F10 cells and incubated at 37 °C for 24 h. The CCK-8 results showed that TBP-N_3 at 2 μg mL^{-1} displayed almost no toxicity in the absence of light irradiation. When the concentrations exceeded 2 μg mL^{-1}, TBP-N_3 displayed increased dark toxicity (Fig. S13A). We used 2 μg mL^{-1} of TBP-N_3 in the following experiment for the cytotoxicity evaluation. Under white light irradiation, TBP-N_3 at 2 μg mL^{-1} exhibited obvious cytotoxic effects, and cell mortality (47 %) was detected (Fig. S13B). In the previous report, even 10 μg mL^{-1} of TBP-2 showed no cytotoxic effects on COS-7 and HLF cells [29]. Excluding the effects caused by different cell types, the phototoxicity of TBP-2 was greatly enhanced due to -N_3 modification. To optimize the time of exposure to light, irradiation at different times was applied to examine cell viability. Ultimately, we chose 6 min as the duration of irradiation in the following experiments (Fig. S13C). TBP@aPD-L1 NPs at 2 μg mL^{-1} with 6 min of irradiation resulted in the death of the cells over 90 %, providing evidence that anti-PD-L1 modification enhanced the cytotoxic effect of TBP-N_3 at the same dose (Fig. 3C). Dead B16F10 cells were also identified by green fluorescent YO-PRO-1 probe after co-incubation of TBP@aPD-L1 NPs with irradiation. YO-PRO-1 is essentially non-fluorescent in the absence of nucleic acids, whereas it emits bright green fluorescence when it enters the cell and binds to DNA after the cell membrane permeability is altered by cell death. The green fluorescence of YO-PRO-1 was significantly increased in the TBP-N_3 + L and TBP@aPD-L1 + L groups compared to the control group (Fig. S13D). The percentage of green fluorescence-positive cells was quantified and Fig. 3D shows that the dead cells in the TBP@aPD-L1 + L group were higher than that in the TBP-N_3 + L group, which indicates that anti-PD-L1 modification improved the cytotoxic effect of TBP-N_3 on B16F10 cells. Furthermore, the cell death was confirmed by FCM with Annexin V/DAPI. The dead/dying population in the TBP-N_3 and TBP@aPD-L1 groups showed slight increase compared to the control group. The proportions of dead/dying in the TBP-N_3 + L and TBP@aPD-L1 + L were remarkably increased and the proportion in the TBP@aPD-L1 + L (~70 %) was significantly higher than that in the TBP-N_3 + L group (~35 %) (Fig. 3E). All these results indicate that TBP-N_3 exhibited strong photocytotoxic effects upon white light irradiation, and modification with anti-PD-L1 enhanced the photocytotoxic effects for more effective PDT.

The photocytotoxic efficiency of the TBP-2-based NPs in our system was substantially improved. As low as 2 μg mL^{-1} of TBP@aPD-L1 NPs killed almost all the tumor cells. In Zhu's study, the bacteria-based hybrid TBP-2 developed could kill 90 % of CT26 cells at a concentration as high as 20 μg mL^{-1} [32]. The high efficiency of our NPs could be attributed to the -N_3 modification, which reduces the positive charge of TBP-2, and the antibody modification on TBP-2, both significantly enhancing the targeting of tumor cells. Moreover, the way we constructed the NPs was highly beneficial for the aggregation of AIEgens. Before antibody modification, we conjugated TBP-N_3 with the linkers to form amphiphiles (Scheme 1A). Amphiphiles are natural to self-assemble to form aggregated cores of TBP-N_3 in biological systems for better performance of AIEgens. Self-assembling nanospheres not only facilitate the loading of antibodies on the NPs, but also greatly increase the loading amount of TBP-2 per unit antibody. In our preliminary experiment, we tried to directly couple antibodies with TBP-2 in the way how to make antibody drug conjugates (ADCs). The amount of TBP-2 coupled to collected antibodies was very low, resulting in particularly poor ROS production efficiency and cell-killing effects. Additional advantages of using self-assembly to construct NPs include simple operation, high reproducibility and high productivity.

3.4. Induction of ICD and DC maturation by TBP@aPD-L1 NPs

In addition to directly causing tumor cell death, PDT also induces ICD of tumor cells, which in turn activates the immune response and synergistically enhances immunotherapeutic effects [22,62,63]. ICD enhances the immunogenicity and antigenicity of tumor cells, thereby increasing the ability of immune cells to recognize and attack tumors [64]. During this process, the dying cells release proinflammatory cytokines and damage-associated molecular patterns (DAMPs) such as surface-exposed calreticulin (CRT) and high mobility group box 1 (HMGB1) protein [65]. DAMPs trigger the maturation of dendritic cells (DCs) and subsequently the mature DCs carrying tumor-specific antigens activate effector T cells to fight against tumors (Fig. 4A) [66]. To investigate whether TBP@aPD-L1 NPs could induce ICD, B16F10 cells were treated with TBP@aPD-L1 NPs under white light irradiation and the ICD-associated markers were assayed. The ELISA results showed that the concentrations of HMGB1 in the supernatant of the TBP-N_3 + L and TBP@aPD-L1 + L groups were significantly increased compared to the TBP-N_3 and TBP@aPD-L1 groups, respectively (Fig. 4B). The expression of membranal CRT was then examined by western blot after PDT treatment. CRT expressions in the TBP-N_3+ L group and TBP@aPD-L1 +

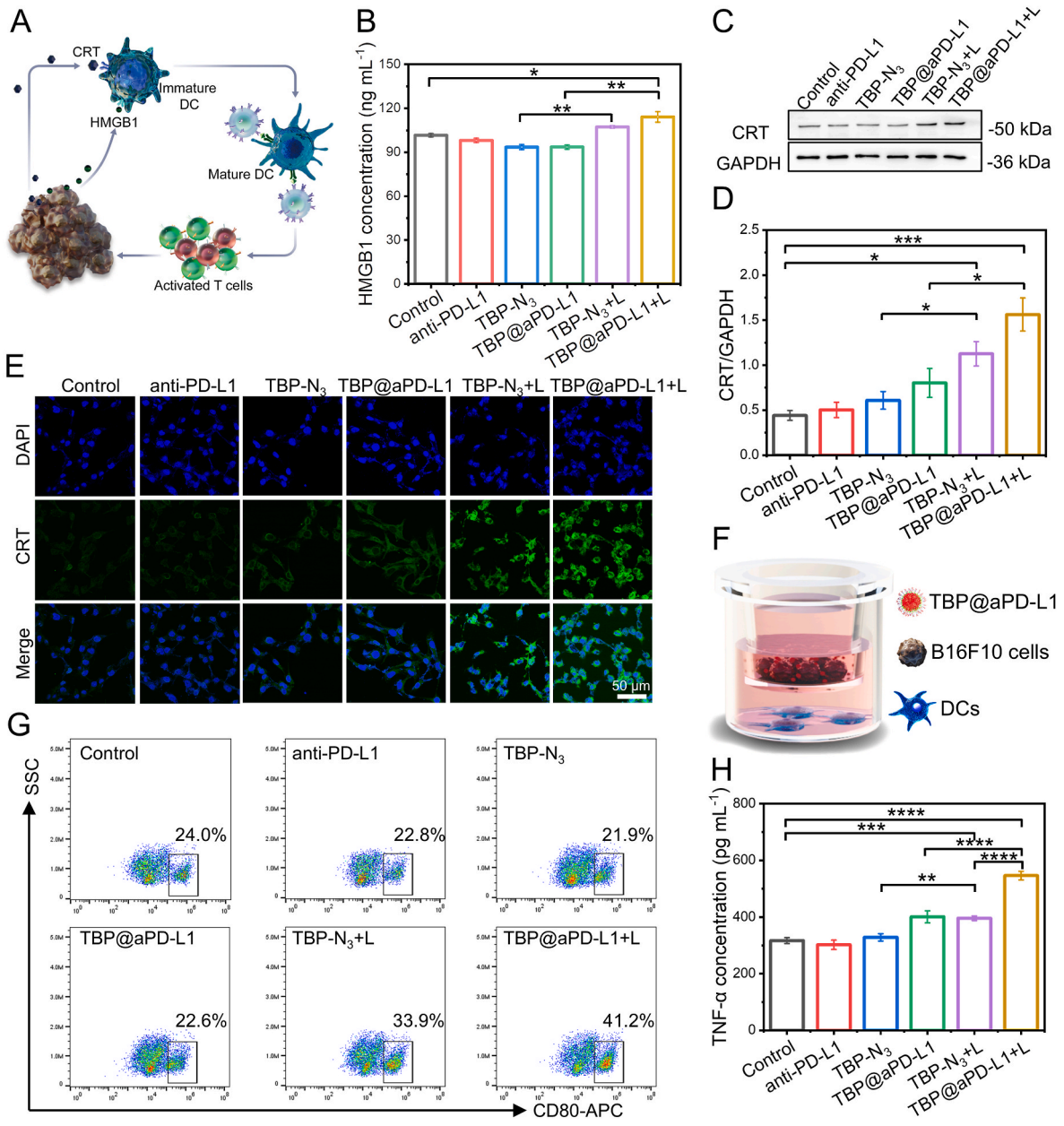

Fig. 4. TBP@aPD-L1 NPs induce ICD and promote the maturation of DCs. **(A)** Schematic illustration of ICD effect on DCs maturation. **(B)** Release of HMGB1 from B16F10 cells after different treatments for 12 h was detected using the ELISA. **(C–D)** Western blot and quantitative analysis of CRT expression on B16F10 cells after different treatments for 12 h. **(E)** CLSM images of CRT expression in B16F10 cells after different treatments. **(F)** Schematic illustration of the coculture system of B16F10 cells and DCs. **(G)** Flow cytometry analysis of DCs maturation was performed after DCs were co-cultured with B16F10 cells for 24 h. **(H)** Contents of the TNF-α in the medium after different treatments for 24 h were quantified using ELISA. "+ L" represents in combination with white light irradiation. Power density: 0.1 W cm^{-2}. Scale bars: 50 μm. The data shows the mean ± SD. (n = 3). Statistical significance was calculated by one-way ANOVA: $^{*}P < 0.05$, $^{**}P < 0.01$, $^{***}P < 0.001$, $^{****}P < 0.0001$.

L groups were increased obviously compared to the TBP-N_3 and TBP@aPD-L1 groups without light irradiation, respectively. CRT expression in the TBP@aPD-L1 + L group was higher than that in the TBP-N_3 + L group (Fig. 4C–D). To assess the exposure of CRT, cell surface proteins were examined for CRT by CLSM. Cells in the TBP-N_3 + L and TBP@aPD-L1 + L groups exhibited higher fluorescence than the other groups, especially in the TBP@aPD-L1 + L group, which was consistent with the western blot results (Fig. 4E). CRT exposure is usually attributed to endoplasmic reticulum (ER) stress caused by PSs [67]. The subcellular distribution of TBP@aPD-L1 NPs in ER was then assessed by co-localization analysis with ER-Tracker. The synchronized intensity profiles of the two co-staining dyes evidenced by CLSM of TBP-2 (Red) and ER-Tracker (Green) in the region of interest demonstrate that TBP@aPD-L1 NPs accumulated in the ER (Fig. S14). All these results indicate that PDT mediated by TBP-N_3 or TBP@aPD-L1 NPs induces ICD in tumor cells, which has great potential to increase the efficacy of immunotherapy in treating cold tumors. In addition, the ICD-inducing effect of TBP@aPD-L1 NPs was obviously stronger than that of TBP-N_3. Since the anti-PD-L1 was not an effective inducer for ICD, the stronger ICD induction observed in the TBP@aPD-L1 + L group was attributed to the more aggregation of TBP-N_3 in tumor cells, facilitated by the targeting effect of anti-PD-L1.

ICD molecules have adjuvant-like effects and act as regulator signals for promoting the maturation of DCs to trigger immune responses against tumors [68]. Therefore, we established a co-culture system of B16F10 cells and mouse bone marrow-derived dendritic cells (BMDCs),

as shown in Fig. 4F, which allowed us to analyze the effect of ICD in B16F10 cells on DC maturation after PDT treatment. CD80 expression, a surface marker of the mature DCs, was examined, which plays a very important role in the process of antigen presentation. The FCM results showed that $CD11c^+CD80^+$ DCs were significantly upregulated in the TBP-N_3 + L (~33.9 %) and TBP@aPD-L1 + L (~41.2 %) groups, compared to the control and the groups without light irradiation. This suggests TBP-N_3-mediated ICD could activate DCs and anti-PD-L1 modification on TBP-N_3 further enhanced this effect (Fig. 4G). The ELISA results also showed a significant increase in the secretion of tumor necrosis factor-α (TNF-α) in DC culture supernatants in the TBP-N_3 + L and TBP@aPD-L1 + L groups, compared to the TBP-N_3 and TBP@aPD-L1 groups, respectively. Moreover, TNF-α secretion in the TBP@aPD-L1 + L group was significantly higher than in the TBP-N_3 + L group (Fig. 4H). All the data suggest that PDT-induced tumor cell death by TBP@aPD-L1 has a strong ability to activate DCs. DCs play an important role in bridging innate and adaptive immune responses to continuously activate cytotoxic T cells [69]. The main reason for the ineffective immune responses is the suppression of various immune cells within the tumor microenvironment, driven by the expression of suppressive molecules by tumor cells [70]. Cancer cells secrete interleukin-6 (IL-6), prostaglandin E2 (PGE2), and some other molecules to inhibit the maturation and differentiation of DCs, resulting in DCs in the tumor microenvironment remaining mostly immature [71,72]. Our NPs exhibit great potential to remodel the tumor microenvironment by enhancing the immunogenicity of dying cancer cells and promoting DC maturation. These NPs offer multiple benefits in treating cancers besides the direct cytotoxic effect of PDT. However, the activating effect on T cells has not been verified *in vitro* due to the limitations of experimental conditions. In the following *in vivo* experiments, we examined the infiltration of T cells in tumor tissues.

3.5. Enhanced synergistic photodynamic therapy and immunotherapy of TBP@aPD-L1 against MM in vivo

To further explore the anti-tumor effects of TBP@aPD-L1 NPs *in vivo*, a syngeneic C57BL/6J mouse model of melanoma was constructed by subcutaneous transplantation of B16F10 cells and the treatment procedures were applied as indicated in Fig. 5A. Instead of transplanting the human melanoma cell line in nude mice, we chose the syngeneic model, involving the inoculation of tumor cell lines of the same background into an inbred mouse strain. In this model, recipient mice have a complete immune system with comprehensive immune activity, and their immune system is compatible with the transplanted cells. This model enables an accurate and authentic reflection of the immune responses in the tumor microenvironment during treatment. First of all, we studied the *in vivo* accumulation of TBP-N_3 or TBP@aPD-L1 NPs over time. Tumor-bearing mice were injected with TBP-N_3 or TBP@aPD-L1 NPs, respectively, followed by the collection of tumors at 6 h, 12 h, and 24 h post injection, and the red fluorescence intensity of TBP-N_3 was detected by immunofluorescence. The red fluorescence was clearly observed in the tumor of both TBP-N_3 or TBP@aPD-L1 NPs treated groups and the fluorescent level was significantly higher in the TBP@aPD-L1 group than that in the TBP-N_3 group (Fig. 5B). This demonstrates that anti-PD-L1 modification promoted the accumulation of PSs at the tumor site. The highest accumulation of fluorescence was observed at 12 h, therefore, this time point was selected for white light irradiation in the subsequent *in vivo* experiments (Fig. 5C). When the tumor reached 100 mm^3, the mice were administrated with different treatments as indicated in Fig. 5D. We monitored the volume of the tumor and body weight every two days. Tumor volume changes during treatment are shown in Fig. 5D. Compared to the control group (PBS), the anti-PD-L1 monotherapy significantly inhibited tumor growth, which is consistent with the previous reports that B16F10 cells are responsive to anti-PD-L1 treatment [73]. TBP@aPD-L1 group exhibited obvious tumor inhibitory effects, suggesting anti-PD-L1 within TBP@aPD-L1 NPs retain their original therapeutic effects. TBP-N_3 alone did not affect tumor growth, while upon white light irradiation, TBP-N_3 significantly inhibited tumor growth, which suggests that TBP-N_3 exerts PDT on tumors *in vivo*. With white light irradiation, the anti-tumor effects in the TBP@aPD-L1 + L group were much more pronounced than those in the TBP-N_3 + L group and the anti-PD-L1 group (Fig. 5D). After 12 days of the treatment, the sizes and weights of dissected tumors were assayed. The same results as shown in Fig. 5D were obtained, and the tumors in the TBP@aPD-L1 + L treated mice were the most significantly inhibited (Fig. 5E–F and Fig. S15). This indicates that TBP@aPD-L1 NPs exerted enhanced synergistic effects of immunotherapy and PDT during the treatment. Subsequently, we assayed ROS levels in the tumor tissues of mice via the DHE probe. Fluorescent staining results showed an obvious increase of ROS in the TBP-N_3 + L and TBP@aPD-L1 + L groups compared to the other groups, suggesting that TBP-N_3 upon irradiation could efficiently generate ROS in tumor tissues. The fluorescent intensity of the DHE probe in the TBP@aPD-L1 + L group was higher than that in the TBP-N_3 + L group, indicating that TBP-N_3, after anti-PD-L1 modification, accumulated more at the tumor site due to anti-PD-L1 targeting and generated more ROS for enhanced PDT (Fig. 5G). Correspondingly, the proliferation and apoptosis of tumor cells were evaluated using markers Ki-67 and terminal deoxynucleotidyl transferase dUTP nick-end labeling (TUNEL), respectively. It was clearly observed that the Ki-67 was most prominently decreased, and the fluorescent TUNEL was most significantly increased in the TBP@aPD-L1 + L group, indicating the proliferation of tumor cells was suppressed and apoptosis of tumor cells was promoted, which is consistent with the results of tumor changes (Fig. 5H). The biosafety of the material is crucial for its potential clinical applications and translation [74,75]. Moreover, there was no obvious weight loss (Fig. S16) and no tissue damage to major organs observed by Hematoxylin & Eosin (H&E) (Fig. S17) during the treatment, demonstrating that our NPs induced no systemic toxicity and manifested good biosafety.

3.6. Immune remodeling of TBP@aPD-L1 against MM in vivo

To verify that PDT by TBP-N_3 remodels immunity during treatment, immunity-related indexes were examined in tumor tissues. CRT was significantly upregulated in the TBP-N_3 + L and TBP@aPD-L1 + L groups compared to those groups without light irradiation, respectively. This finding indicates that TBP-N_3 successfully induced ICD *in vivo* after white light irradiation. Moreover, CRT expression in the TBP@aPD-L1 + L group was significantly stronger than that in the TBP-N_3 + L group (Fig. 6A–B). The stronger CRT expression in the TBP@aPD-L1 + L group was attributed to the increased aggregation of TBP-N_3 in tumors, facilitated by the targeting effect of anti-PD-L1 [76]. Furthermore, we examined the infiltration of DCs and T cells in tumors. Activated DCs were marked by $CD11c^+CD80^+$ for CLSM assay. Fig. 6C–D showed that both TBP-N_3 + L and TBP@aPD-L1 + L groups exhibited increased $CD11c^+CD80^+$ staining compared to TBP-N_3 and TBP@aPD-L1 groups, respectively, which indicates that TBP-N_3 with light irradiation could promote the maturation of DCs. The proportion of $CD11c^+CD80^+$ cells in the TBP@aPD-L1 + L group was significantly higher than that in the TBP-N_3 + L group. Activated DCs produce a wide range of chemokines to recruit T cells, which are immune effector cells for killing tumor cells [77]. Therefore, we further examined the extent of T cell infiltration. Our immunofluorescence results in Fig. 6E–G for T cells revealed that there was an obvious increase of $CD4^+$ and $CD8^+$ T cells in both the anti-PD-L1 group and TBP@aPD-L1 group compared to the control. This is consistent with the conceptual consensus that PD-L1 blockade increases T cell infiltration and enhances the cytotoxic function of tumor infiltrating lymphocytes (TILs) [78]. The proportions of $CD4^+$ and $CD8^+$ T cells in the TBP-N_3 + L group were significantly higher than those in the TBP-N_3 group, which suggests that TBP-N_3 mediated PDT increased T cell infiltration. Compared with all other groups, the TBP@aPD-L1 + L group showed the highest percentages of $CD4^+$ and $CD8^+$ T cells to the

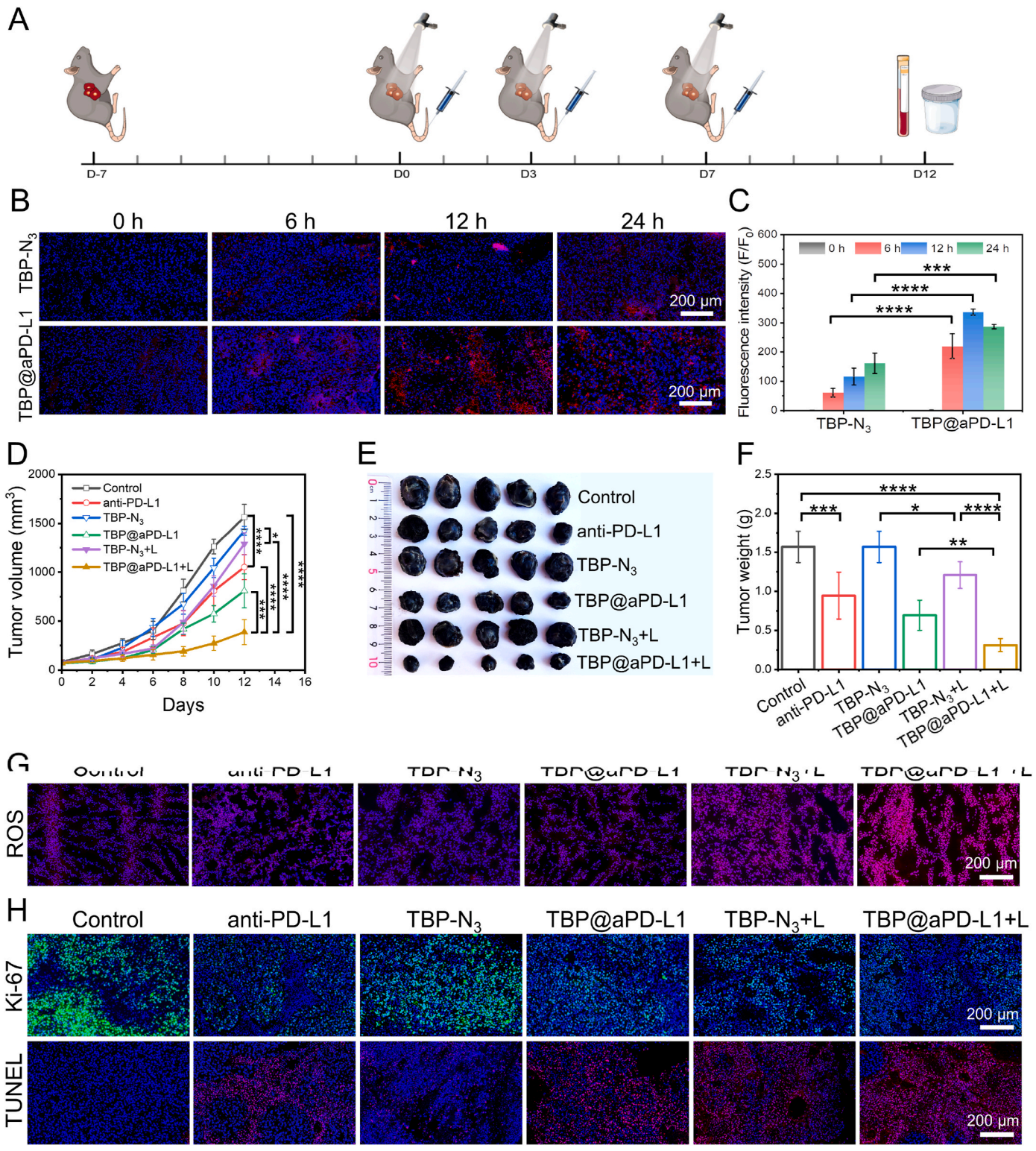

Fig. 5. Effective anti-tumor performance of TBP@aPD-L1 NPs in the B16F10 tumor model. **(A)** Timeline of the combined therapy *in vivo*. **(B)** Fluorescence intensity of tumor tissues at different time periods after TBP-N_3 or TBP@aPD-L1 NPs injection. **(C)** Quantification of fluorescence intensity at different time points in tumor tissues. **(D)** Tumor volume of tumor-bearing mice as a function of time post different treatments during 12 days. **(E)** Photographs of tumors collected from different treatment groups after 12 days. **(F)** Corresponding tumor weights of mice at 12 days after different treatments. **(G–H)** ROS, Ki-67 and TUNEL staining of tumors after the mice were treated for 12 days in different groups. "+ L" represents in combination with white light irradiation. Power density: 0.1 W cm^{-2}. Scale bars: 200 μm. The data shows the mean ± SD. (n = 5). Statistical significance was calculated by one-way ANOVA: $^{*}P < 0.05$, $^{**}P < 0.01$, $^{***}P < 0.001$, $^{****}P < 0.0001$ and ns: no significance.

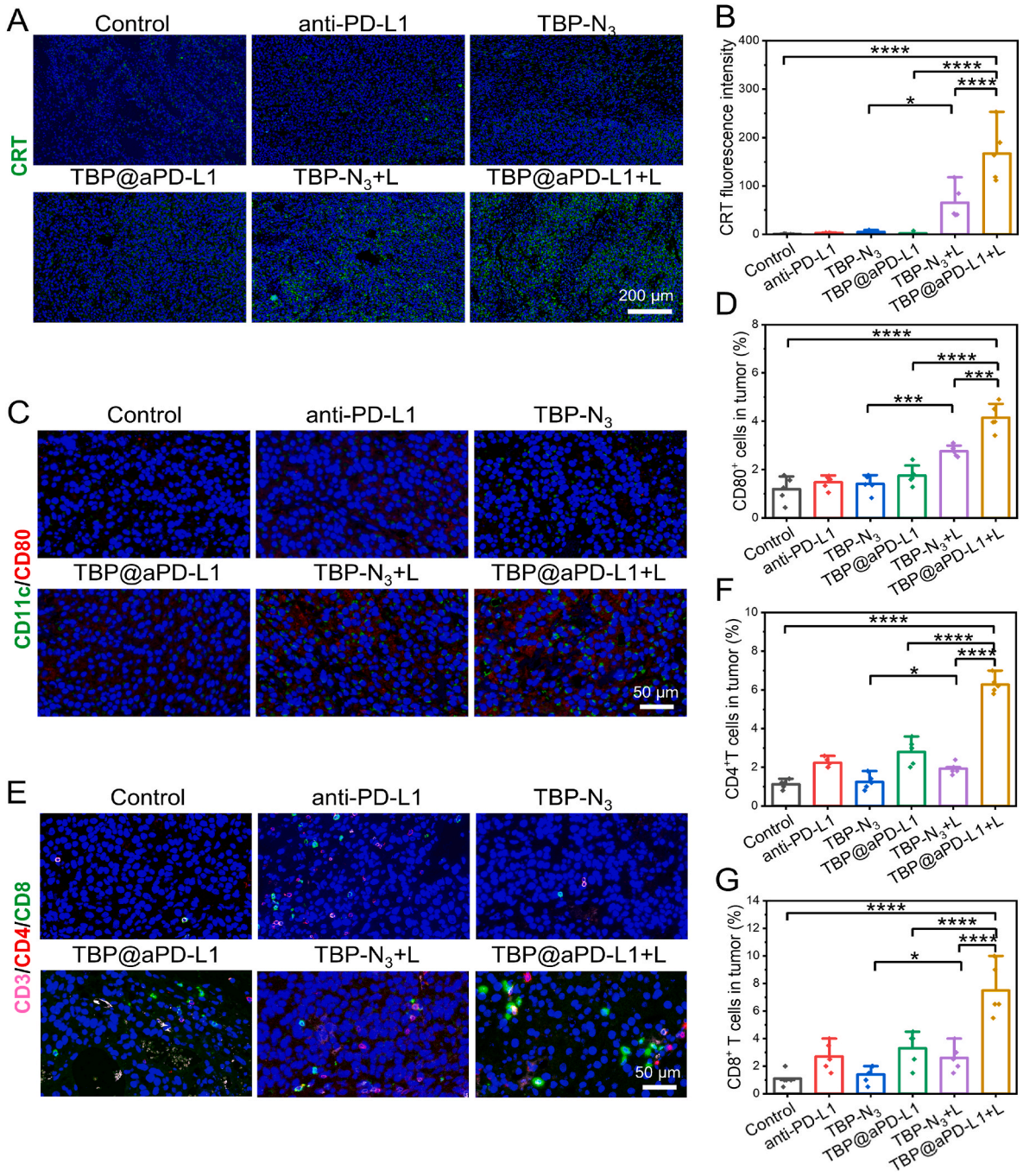

Fig. 6. The anti-tumor immune profile of TBP@aPD-L1 NPs in the B16F10 tumor model. **(A–B)** Immunofluorescence staining and quantitative analysis of CRT after the mice were treated for 12 days in different treatments. Scale bars: 200 μm. **(C)** Immunofluorescence staining of $CD11c^+$ and $CD80^+$ in tumor tissues after the mice were treated for 12 days in different groups (Green: $CD11c^+$ Red: $CD80^+$). **(D)** Quantitative analysis of $CD80^+$ in tumor tissues after different treatments. **(E)** Immunofluorescence staining of $CD3^+$ $CD4^+$ and $CD8^+$ T cells in tumor tissues after the mice were treated for 12 days in different groups (Pink: $CD3^+$ Red: $CD4^+$ Green: $CD8^+$). **(F)** Quantitative analysis of $CD4^+$ T cells in tumor tissues after different treatments. **(G)** Quantitative analysis of $CD8^+$ T cells in tumor tissues after different treatments. Scale bars: 50 μm "+ L" represents in combination with white light irradiation. Power density: 0.1 W cm^{-2}. The data shows the mean ± SD. (n = 5). Statistical significance was calculated by one-way ANOVA: $^*P < 0.05$, $^{***}P < 0.001$, $^{****}P < 0.0001$.

total cells (6 % and 7.5 %, respectively) in tumors. In particular, the proportions of $CD4^+$ and $CD8^+$ T cells in the TBP@aPD-L1 + L group significantly increased compared to those in the anti-PD-L1 and TBP@aPD-L1 groups, which indicates that TBP@aPD-L1 NPs enhanced immune remodeling compared to anti-PD-L1 alone (Fig. 6E–G). Hence, TBP@aPD-L1-induced ICD remodeled the immune status by recruitment and activation of DCs and T cells which was beneficial for immunotherapy. In addition to inducing direct tumor cell death, TBP@aPD-L1 NPs mediated PDT could act as an efficient inducer to promote the anti-tumor immunity of PD-L1 blockade. Summarily, all the results suggest that our NPs achieved more effective anti-tumor effects than TBP-N_3 + L or anti-PD-L1 alone, ultimately realizing "1 + 1 > 2" enhanced PDT-ICI synergistic therapy. This "all in one" nanoplatform offers multiple benefits in treating cancer and holds promise for enhancing the immunogenicity of dying cancer cells induced by PDT based on AIEgens. Thus, our study provides a multimodal strategy for the treatment of MM by simultaneously enhancing PDT and immunotherapy and serves as an important reference for addressing the poor

clinical response to immunotherapy.

4. Conclusion

In conclusion, we have successfully developed multimodal therapeutic TBP@aPD-L1 NPs based on AIEgens. These NPs exerted effective anti-tumor effects on MM by enhancing the synergy of PDT and immunotherapy. Notably, the AIE properties, type I ROS generation capacity and efficient tumor-targeting ability of our NPs enabled them to function as potent PSs with high ROS production, significantly enhancing the efficacy of PDT. Moreover, the TBP@aPD-L1-mediated PDT induced strong ICD, resulting in extensive immune remodeling. The combination of PDT and immunotherapy facilitated DC maturation, increased T cell infiltration, and converted "cold" tumors into "hot" tumors. TBP@aPD-L1 NPs ultimately improved the tumor cell responsiveness to anti-PD-L1 therapy, resulting in enhanced immunotherapeutic outcomes. Therefore, we provided a targeted nanoplatform based on AIEgens to enhance the efficiency of ICIs, which offers robust photoimmunotherapeutic capabilities by combining the simultaneously enhanced PDT and immunotherapy. It offers a fresh perspective that encourages further investigation into the utilization of PDT to address the clinical challenges associated with ICI application.

CRediT authorship contribution statement

Lu Li: Writing – original draft, Methodology, Investigation, Data curation, Conceptualization. **Qing Xu:** Writing – original draft, Investigation, Conceptualization. **Xiuzhen Zhang:** Writing – original draft, Methodology. **Yuan Jiang:** Methodology. **La Zhang:** Validation, Investigation. **Jiao Guo:** Methodology. **Haichuan Liu:** Methodology. **Bin Jiang:** Methodology. **Shenglong Li:** Validation, Supervision, Methodology. **Qiling Peng:** Writing – review & editing, Supervision, Funding acquisition. **Ning Jiang:** Writing – original draft, Validation, Supervision. **Jianwei Wang:** Writing – review & editing, Validation, Supervision, Funding acquisition, Conceptualization.

Declaration of competing interest

The authors declare that they have no known competing financial interests or personal relationships that could have appeared to influence the work reported in this paper.

Acknowledgements

We express our gratitude to Prof. Wenjun Miao for his technical assistance and to Xia Zhang (Molecular Medicine and Cancer Research Center, Chong Qing Medical University) for assistance with fluorescence microscopy. We would like to express our special thanks to Prof. Benzhong Tang and Prof. Zhiming Wang from AIE Institute of South China University of Technology for providing TBP-2. This work was supported by the Natural Science Foundation of Chongqing City (grant numbers CSTB2022NSCQ-MSX0054), the Science and Technology Research Program of Chongqing Municipal Education Commission (grant numbers KJQN202300478) and the National Natural Science Foundation of China (grant numbers 32460233).

Appendix A. Supplementary data

Supplementary data to this article can be found online at https://doi.org/10.1016/j.mtbio.2024.101387.

Data availability

Data will be made available on request.

References

[1] L. Stătescu, L.M. Trandafir, E. Țarcă, M. Moscalu, M.M. Leon Constantin, L. I. Butnariu, M.F. Trandafirescu, M.C. Tîrnovanu, R. Heredea, A.V. Pătrașcu, D. Botezat, E. Cojocaru, Advancing cancer Research: current knowledge on cutaneous neoplasia, Int. J. Mol. Sci. 24 (13) (2023), https://doi.org/10.3390/ijms241311176.

[2] O. Michielin, A.C.J. van Akkooi, P.A. Ascierto, R. Dummer, U. Keilholz, Cutaneous melanoma: ESMO Clinical Practice Guidelines for diagnosis, treatment and follow-up, Ann. Oncol. 30 (12) (2019) 1884–1901, https://doi.org/10.1093/annonc/mdz411.

[3] M. Arnold, D. Singh, M. Laversanne, J. Vignat, S. Vaccarella, F. Meheus, A.E. Cust, E. de Vries, D.C. Whiteman, F. Bray, Global burden of cutaneous melanoma in 2020 and projections to 2040, JAMA Dermatol 158 (5) (2022) 495–503, https://doi.org/10.1001/jamadermatol.2022.0160.

[4] K. Eddy, S. Chen, Overcoming immune evasion in melanoma, Int. J. Mol. Sci. 21 (23) (2020), https://doi.org/10.3390/ijms21238984.

[5] R.R. Braeuer, I.R. Watson, C.J. Wu, A.K. Mobley, T. Kamiya, E. Shoshan, M. Bar-Eli, Why is melanoma so metastatic? Pigment Cell Melanoma Res 27 (1) (2014) 19–36, https://doi.org/10.1111/pcmr.12172.

[6] L. Skudalski, R. Waldman, P.E. Kerr, J.M. Grant-Kels, Melanoma: an update on systemic therapies, J. Am. Acad. Dermatol. 86 (3) (2022) 515–524, https://doi.org/10.1016/j.jaad.2021.09.075.

[7] G.V. Long, A.M. Menzies, R.A. Scolyer, Neoadjuvant checkpoint immunotherapy and melanoma: the time is now, J. Clin. Oncol. 41 (17) (2023) 3236–3248, https://doi.org/10.1200/jco.22.02575.

[8] W. Wagstaff, R.N. Mwamba, K. Grullon, M. Armstrong, P. Zhao, B. Hendren-Santiago, K.H. Qin, A.J. Li, D.A. Hu, A. Youssef, R.R. Reid, H.H. Luu, L. Shen, T. C. He, R.C. Haydon, Melanoma: molecular genetics, metastasis, targeted therapies, immunotherapies, and therapeutic resistance, Genes Dis 9 (6) (2022) 1608–1623, https://doi.org/10.1016/j.gendis.2022.04.004.

[9] M. Yi, X. Zheng, M. Niu, S. Zhu, H. Ge, K. Wu, Combination strategies with PD-1/PD-L1 blockade: current advances and future directions, Mol. Cancer 21 (1) (2022) 28, https://doi.org/10.1186/s12943-021-01489-2.

[10] Z. Zhou, W. Luo, C. Zheng, H. Wang, R. Hu, H. Deng, J. Shen, Mitochondrial metabolism blockade nanoadjuvant reversed immune-resistance microenvironment to sensitize albumin-bound paclitaxel-based chemo-immunotherapy, Acta Pharm. Sin. B 14 (9) (2024) 4087–4101, https://doi.org/10.1016/j.apsb.2024.05.028.

[11] L. Yi, X. Jiang, Z. Zhou, W. Xiong, F. Xue, Y. Liu, H. Xu, B. Fan, Y. Li, J. Shen, A hybrid nanoadjuvant simultaneously depresses PD-L1/TGF-beta1 and activates cGAS-STING pathway to overcome radio-immunotherapy resistance, Adv Mater 36 (15) (2024) e2304328, https://doi.org/10.1002/adma.202304328.

[12] A. Akinleye, Z. Rasool, Immune checkpoint inhibitors of PD-L1 as cancer therapeutics, J. Hematol. Oncol. 12 (1) (2019) 92, https://doi.org/10.1186/s13045-019-0779-5.

[13] S.L. Topalian, J.M. Taube, R.A. Anders, D.M. Pardoll, Mechanism-driven biomarkers to guide immune checkpoint blockade in cancer therapy, Nat. Rev. Cancer 16 (5) (2016) 275–287, https://doi.org/10.1038/nrc.2016.36.

[14] S. Kim, S.A. Kim, G.H. Nam, Y. Hong, G.B. Kim, Y. Choi, S. Lee, Y. Cho, M. Kwon, C. Jeong, S. Kim, I.S. Kim, In situ immunogenic clearance induced by a combination of photodynamic therapy and rho-kinase inhibition sensitizes immune checkpoint blockade response to elicit systemic antitumor immunity against intraocular melanoma and its metastasis, J Immunother Cancer 9 (1) (2021), https://doi.org/10.1136/jitc-2020-001481.

[15] A.C. Guidon, L.B. Burton, B.K. Chwalisz, J. Hillis, T.H. Schaller, A.A. Amato, A. Betof Warner, P.K. Brastianos, T.A. Cho, S.L. Clardy, J.V. Cohen, J. Dietrich, M. Dougan, C.T. Doughty, D. Dubey, J.M. Gelfand, J.T. Guptill, D.B. Johnson, V. C. Juel, R. Kadish, N. Kolb, N.R. LeBoeuf, J. Linnoila, A.L. Mammen, M. Martinez-Lage, M.J. Mooradian, J. Naidoo, T.G. Neilan, D.A. Reardon, K.M. Rubin, B. D. Santomasso, R.J. Sullivan, N. Wang, K. Woodman, L. Zubiri, W.C. Louv, K. L. Reynolds, Consensus disease definitions for neurologic immune-related adverse events of immune checkpoint inhibitors, J Immunother Cancer 9 (7) (2021), https://doi.org/10.1136/jitc-2021-002890.

[16] J.D. Wolchok, V. Chiarion-Sileni, R. Gonzalez, P. Rutkowski, J.J. Grob, C.L. Cowey, C.D. Lao, J. Wagstaff, D. Schadendorf, P.F. Ferrucci, M. Smylie, R. Dummer, A. Hill, D. Hogg, J. Haanen, M.S. Carlino, O. Bechter, M. Maio, I. Marquez-Rodas, M. Guidoboni, G. McArthur, C. Lebbé, P.A. Ascierto, G.V. Long, J. Cebon, J. Sosman, M.A. Postow, M.K. Callahan, D. Walker, L. Rollin, R. Bhore, F.S. Hodi, J. Larkin, Overall survival with combined nivolumab and ipilimumab in advanced melanoma, N. Engl. J. Med. 377 (14) (2017) 1345–1356, https://doi.org/10.1056/NEJMoa1709684.

[17] F.S. Hodi, S.J. O'Day, D.F. McDermott, R.W. Weber, J.A. Sosman, J.B. Haanen, R. Gonzalez, C. Robert, D. Schadendorf, J.C. Hassel, W. Akerley, A.J. van den Eertwegh, J. Lutzky, P. Lorigan, J.M. Vaubel, G.P. Linette, D. Hogg, C. H. Ottensmeier, C. Lebbé, C. Peschel, I. Quirt, J.I. Clark, J.D. Wolchok, J.S. Weber, J. Tian, M.J. Yellin, G.M. Nichol, A. Hoos, W.J. Urba, Improved survival with ipilimumab in patients with metastatic melanoma, N. Engl. J. Med. 363 (8) (2010) 711–723, https://doi.org/10.1056/NEJMoa1003466.

[18] J. Zhao, Y. Gao, R. Huang, C. Chi, Y. Sun, G. Xu, X.H. Xia, S. Gou, Design of near-infrared-triggered metallo-photosensitizers via a self-assembly-induced vibronic decoupling strategy, J. Am. Chem. Soc. 145 (21) (2023) 11633–11642, https://doi.org/10.1021/jacs.3c01645.

[19] J. Xie, Y. Wang, W. Choi, P. Jangili, Y. Ge, Y. Xu, J. Kang, L. Liu, B. Zhang, Z. Xie, J. He, N. Xie, G. Nie, H. Zhang, J.S. Kim, Overcoming barriers in photodynamic

therapy harnessing nano-formulation strategies, Chem. Soc. Rev. 50 (16) (2021) 9152–9201, https://doi.org/10.1039/d0cs01370f.
[20] L. Xie, H. Yang, X. Wu, L. Wang, B. Zhu, Y. Tang, M. Bai, L. Li, C. Cheng, T. Ma, Ti-MOF-based biosafety materials for efficient and long-life disinfection via synergistic photodynamic and photothermal effects, Biosafety and Health 4 (2) (2022) 135–146, https://doi.org/10.1016/j.bsheal.2022.02.001.
[21] B. Ji, M. Wei, B. Yang, Recent advances in nanomedicines for photodynamic therapy (PDT)-driven cancer immunotherapy, Theranostics 12 (1) (2022) 434–458, https://doi.org/10.7150/thno.67300.
[22] S. Zhang, J. Wang, Z. Kong, X. Sun, Z. He, B. Sun, C. Luo, J. Sun, Emerging photodynamic nanotherapeutics for inducing immunogenic cell death and potentiating cancer immunotherapy, Biomaterials 282 (2022) 121433, https://doi.org/10.1016/j.biomaterials.2022.121433.
[23] A. Song, Y. Wang, J. Xu, X. Wang, Y. Wu, H. Wang, C. Yao, H. Dai, Y. Zhang, Q. Wang, C. Wang, Yeast nanoparticle-powered tumor photodynamic-immunotherapy, Nano Today 54 (2024), https://doi.org/10.1016/j.nantod.2023.102109.
[24] X. Gao, G. Lei, B. Wang, Z. Deng, J. Karges, H. Xiao, D. Tan, Encapsulation of platinum prodrugs into PC7A polymeric nanoparticles combined with immune checkpoint inhibitors for therapeutically enhanced multimodal chemotherapy and immunotherapy by activation of the STING pathway, Adv. Sci. 10 (4) (2022), https://doi.org/10.1002/advs.202205241.
[25] X. Cheng, J. Gao, Y. Ding, Y. Lu, Q. Wei, D. Cui, J. Fan, X. Li, E. Zhu, Y. Lu, Q. Wu, L. Li, W. Huang, Multi-functional liposome: a powerful theranostic nano-platform enhancing photodynamic therapy, Adv. Sci. 8 (16) (2021) e2100876, https://doi.org/10.1002/advs.202100876.
[26] J. Mei, N.L. Leung, R.T. Kwok, J.W. Lam, B.Z. Tang, Aggregation-induced emission: together we shine, united we soar, Chem Rev 115 (21) (2015) 11718–11940, https://doi.org/10.1021/acs.chemrev.5b00263.
[27] Y. Gao, Q.C. Zheng, S. Xu, Y. Yuan, X. Cheng, S. Jiang, Kenry, Q. Yu, Z. Song, B. Liu, M. Li, Theranostic nanodots with aggregation-induced emission characteristic for targeted and image-guided photodynamic therapy of hepatocellular carcinoma, Theranostics 9 (5) (2019) 1264–1279, https://doi.org/10.7150/thno.29101.
[28] Y. Yu, H. Jia, Y. Liu, L. Zhang, G. Feng, B.Z. Tang, Recent progress in type I aggregation-induced emission photosensitizers for photodynamic therapy, Molecules 28 (1) (2022), https://doi.org/10.3390/molecules28010332.
[29] X. Shi, S.H.P. Sung, J.H.C. Chau, Y. Li, Z. Liu, R.T.K. Kwok, J. Liu, P. Xiao, J. Zhang, B. Liu, J.W.Y. Lam, B.Z. Tang, G. Killing, (+) or G(−) bacteria? The important role of molecular charge in AIE-active photosensitizers, Small Methods 4 (7) (2020), https://doi.org/10.1002/smtd.202000046.
[30] H. Dewitte, R. Verbeke, K. Breckpot, R.E. Vandenbroucke, C. Libert, S.C. De Smedt, I. Lentacker, Choose your models wisely: how different murine bone marrow-derived dendritic cell protocols influence the success of nanoparticulate vaccines in vitro, J Control Release 195 (2014) 138–146, https://doi.org/10.1016/j.jconrel.2014.06.024.
[31] M. Sauter, R.J. Sauter, H. Nording, M. Olbrich, F. Emschermann, H.F. Langer, Protocol to isolate and analyze mouse bone marrow derived dendritic cells (BMDC), STAR Protoc 3 (3) (2022) 101664, https://doi.org/10.1016/j.xpro.2022.101664.
[32] D. Zhu, J. Zhang, G. Luo, Y. Duo, B.Z. Tang, Bright bacterium for hypoxia-tolerant photodynamic therapy against orthotopic colon tumors by an interventional method, Adv. Sci. 8 (15) (2021) e2004769, https://doi.org/10.1002/advs.202004769.
[33] S. Ning, M. Lyu, D. Zhu, J.W.Y. Lam, Q. Huang, T. Zhang, B.Z. Tang, Type-I AIE photosensitizer loaded biomimetic system boosting cuproptosis to inhibit breast cancer metastasis and rechallenge, ACS Nano 17 (11) (2023) 10206–10217, https://doi.org/10.1021/acsnano.3c00326.
[34] X. Zheng, D. Wang, W. Xu, S. Cao, Q. Peng, B.Z. Tang, Charge control of fluorescent probes to selectively target the cell membrane or mitochondria: theoretical prediction and experimental validation, Mater. Horiz. 6 (10) (2019) 2016–2023, https://doi.org/10.1039/C9MH00906J.
[35] S. Ning, T. Zhang, M. Lyu, J.W.Y. Lam, D. Zhu, Q. Huang, B.Z. Tang, A type I AIE photosensitiser-loaded biomimetic nanosystem allowing precise depletion of cancer stem cells and prevention of cancer recurrence after radiotherapy, Biomaterials 295 (2023) 122034, https://doi.org/10.1016/j.biomaterials.2023.122034.
[36] J. Lee, S.Z. Hassan, S. Lee, H.R. Sim, D.S. Chung, Azide-functionalized ligand enabling organic-inorganic hybrid dielectric for high-performance solution-processed oxide transistors, Nat. Commun. 13 (1) (2022) 7021, https://doi.org/10.1038/s41467-022-34772-x.
[37] C. Dizman, C. Altinkok, M.A. Tasdelen, Synthesis of self-curable polysulfone containing pendant benzoxazine units via CuAAC click chemistry, Des. Monomers Polym. 20 (1) (2017) 293–299, https://doi.org/10.1080/15685551.2016.1257379.
[38] D. Scherrer, D. Vogel, U. Drechsler, A. Olziersky, C. Sparr, M. Mayor, E. Lörtscher, Monitoring solid-phase reactions in self-assembled monolayers by surface-enhanced Raman spectroscopy, Angew Chem. Int. Ed. Engl. 60 (33) (2021) 17981–17988, https://doi.org/10.1002/anie.202102319.
[39] J. Osuofa, S.M. Husson, Preparation of protein A membrane adsorbers using strain-promoted, copper-free dibenzocyclooctyne (DBCO)-Azide click chemistry, Membranes 13 (10) (2023), https://doi.org/10.3390/membranes13100824.
[40] A. Bansal, M.C. Simon, Glutathione metabolism in cancer progression and treatment resistance, J. Cell Biol. 217 (7) (2018) 2291–2298, https://doi.org/10.1083/jcb.201804161.
[41] F. Wu, Y. Du, J. Yang, B. Shao, Z. Mi, Y. Yao, Y. Cui, F. He, Y. Zhang, P. Yang, Peroxidase-like active nanomedicine with dual glutathione depletion property to restore oxaliplatin chemosensitivity and promote programmed cell death, ACS Nano 16 (3) (2022) 3647–3663, https://doi.org/10.1021/acsnano.1c06777.
[42] L.H. Fu, Y. Wan, C. Qi, J. He, C. Li, C. Yang, H. Xu, J. Lin, P. Huang, Nanocatalytic theranostics with glutathione depletion and enhanced reactive oxygen species generation for efficient cancer therapy, Adv Mater 33 (7) (2021) e2006892, https://doi.org/10.1002/adma.202006892.
[43] D. Chen, Y. Feng, Recent progress of glutathione (GSH) specific fluorescent probes: molecular design, photophysical property, recognition mechanism and bioimaging, Crit. Rev. Anal. Chem. 52 (3) (2020) 649–666, https://doi.org/10.1080/10408347.2020.1819193.
[44] C.-Y. Cui, B. Li, X.-C. Su, Real-time monitoring of the level and activity of intracellular glutathione in live cells at atomic resolution by 19F-NMR, ACS Cent. Sci. 9 (8) (2023) 1623–1632, https://doi.org/10.1021/acscentsci.3c00385.
[45] J. Qi, H. Ou, Q. Liu, D. Ding, Gathering brings strength: how organic aggregates boost disease phototheranostics, Aggregate 2 (1) (2021) 95–113, https://doi.org/10.1002/agt2.25.
[46] G. Gunaydin, M.E. Gedik, S. Ayan, Photodynamic therapy-current limitations and novel approaches, Front. Chem. 9 (2021) 691697, https://doi.org/10.3389/fchem.2021.691697.
[47] C. Zhang, X. Hu, L. Jin, L. Lin, H. Lin, Z. Yang, W. Huang, Strategic design of conquering hypoxia in tumor for advanced photodynamic therapy, Adv Healthc Mater 12 (24) (2023) e2300530, https://doi.org/10.1002/adhm.202300530.
[48] R. Liang, L. Liu, H. He, Z. Chen, Z. Han, Z. Luo, Z. Wu, M. Zheng, Y. Ma, L. Cai, Oxygen-boosted immunogenic photodynamic therapy with gold nanocages@manganese dioxide to inhibit tumor growth and metastases, Biomaterials 177 (2018) 149–160, https://doi.org/10.1016/j.biomaterials.2018.05.051.
[49] D.W. Zheng, B. Li, C.X. Li, J.X. Fan, Q. Lei, C. Li, Z. Xu, X.Z. Zhang, Carbon-dot-decorated carbon nitride nanoparticles for enhanced photodynamic therapy against hypoxic tumor via water splitting, ACS Nano 10 (9) (2016) 8715–8722, https://doi.org/10.1021/acsnano.6b04156.
[50] M. Kang, Z. Zhang, W. Xu, H. Wen, W. Zhu, Q. Wu, H. Wu, J. Gong, Z. Wang, D. Wang, B.Z. Tang, Good steel used in the blade: well-tailored type-I photosensitizers with aggregation-induced emission characteristics for precise nuclear targeting photodynamic therapy, Adv. Sci. 8 (14) (2021) e2100524, https://doi.org/10.1002/advs.202100524.
[51] K. Plaetzer, B. Krammer, J. Berlanda, F. Berr, T. Kiesslich, Photophysics and photochemistry of photodynamic therapy: fundamental aspects, Lasers Med Sci 24 (2) (2009) 259–268, https://doi.org/10.1007/s10103-008-0539-1.
[52] Q. Xie, Z. Li, Y. Liu, D. Zhang, M. Su, H. Niitsu, Y. Lu, R.J. Coffey, M. Bai, Translocator protein-targeted photodynamic therapy for direct and abscopal immunogenic cell death in colorectal cancer, Acta Biomater. 134 (2021) 716–729, https://doi.org/10.1016/j.actbio.2021.07.052.
[53] M. Liu, Y. Chen, Y. Guo, H. Yuan, T. Cui, S. Yao, S. Jin, H. Fan, C. Wang, R. Xie, W. He, Z. Guo, Golgi apparatus-targeted aggregation-induced emission luminogens for effective cancer photodynamic therapy, Nat. Commun. 13 (1) (2022) 2179, https://doi.org/10.1038/s41467-022-29872-7.
[54] P. Lasso, A. Gomez-Cadena, C. Urueña, A. Donda, A. Martinez-Usatorre, P. Romero, A. Barreto, S. Fiorentino, An immunomodulatory gallotanin-rich fraction from Caesalpinia spinosa enhances the therapeutic effect of anti-PD-L1 in melanoma, Front. Immunol. 11 (2020) 584959, https://doi.org/10.3389/fimmu.2020.584959.
[55] H. Tian, G. Shi, Q. Wang, Y. Li, Q. Yang, C. Li, G. Yang, M. Wu, Q. Xie, S. Zhang, Y. Yang, R. Xiang, D. Yu, Y. Wei, H. Deng, A novel cancer vaccine with the ability to simultaneously produce anti-PD-1 antibody and GM-CSF in cancer cells and enhance Th1-biased antitumor immunity, Signal Transduct Target Ther 1 (2016) 16025, https://doi.org/10.1038/sigtrans.2016.25.
[56] J. Qi, Y. Fang, R.T.K. Kwok, X. Zhang, X. Hu, J.W.Y. Lam, D. Ding, B.Z. Tang, Highly stable organic small molecular nanoparticles as an advanced and biocompatible phototheranostic agent of tumor in living mice, ACS Nano 11 (7) (2017) 7177–7188, https://doi.org/10.1021/acsnano.7b03062.
[57] G. Xu, C. Li, C. Chi, L. Wu, Y. Sun, J. Zhao, X.H. Xia, S. Gou, A supramolecular photosensitizer derived from an Arene-Ru(II) complex self-assembly for NIR activated photodynamic and photothermal therapy, Nat. Commun. 13 (1) (2022) 3064, https://doi.org/10.1038/s41467-022-30721-w.
[58] M. Reda, W. Ngamcherdtrakul, M.A. Nelson, N. Siriwon, R. Wang, H.Y. Zaidan, D. S. Bejan, S. Reda, N.H. Hoang, N.A. Crumrine, J.P.C. Rehwaldt, A. Bindal, G. B. Mills, J.W. Gray, W. Yantasee, Development of a nanoparticle-based immunotherapy targeting PD-L1 and PLK1 for lung cancer treatment, Nat. Commun. 13 (1) (2022) 4261, https://doi.org/10.1038/s41467-022-31926-9.
[59] J. Karges, Combination of chemistry and material science to overcome health problems, Biosafety and Health 4 (2) (2022) 64–65, https://doi.org/10.1016/j.bsheal.2022.03.004.
[60] X. Jiang, L. Yi, C. Li, H. Wang, W. Xiong, Y. Li, Z. Zhou, J. Shen, Mitochondrial disruption nanosystem simultaneously depressed programmed death ligand-1 and transforming growth factor-β to overcome photodynamic immunotherapy resistance, ACS Nano 18 (4) (2024) 3331–3348, https://doi.org/10.1021/acsnano.3c10117.
[61] Z. Zhou, H. Wang, J. Li, X. Jiang, Z. Li, J. Shen, Recent progress, perspectives, and issues of engineered PD-L1 regulation nano-system to better cure tumor: a review, Int. J. Biol. Macromol. 254 (Pt 2) (2024) 127911, https://doi.org/10.1016/j.ijbiomac.2023.127911.
[62] M. Zhang, Y. Zhao, H. Ma, Y. Sun, J. Cao, How to improve photodynamic therapy-induced antitumor immunity for cancer treatment? Theranostics 12 (10) (2022) 4629–4655, https://doi.org/10.7150/thno.72465.

[63] Q. Zhao, G. Liang, B. Guo, W. Wang, C. Yang, D. Chen, F. Yang, H. Xiao, N. Xing, Polyphotosensitizer-based nanoparticles with Michael addition acceptors inhibiting GST activity and cisplatin deactivation for enhanced chemotherapy and photodynamic immunotherapy, Adv. Sci. 10 (13) (2023), https://doi.org/10.1002/advs.202300175.

[64] B. Wang, J. Zhou, R. Li, D. Tang, Z. Cao, C. Xu, H. Xiao, Activating CD8+ T cells by Pt(IV) prodrug-based nanomedicine and aPD-L1 antibody for enhanced cancer immunotherapy, Adv. Mater. 36 (21) (2024), https://doi.org/10.1002/adma.202311640.

[65] D. Xie, Q. Wang, G. Wu, Research progress in inducing immunogenic cell death of tumor cells, Front. Immunol. 13 (2022) 1017400, https://doi.org/10.3389/fimmu.2022.1017400.

[66] Z. Li, X. Lai, S. Fu, L. Ren, H. Cai, H. Zhang, Z. Gu, X. Ma, K. Luo, Immunogenic cell death activates the tumor immune microenvironment to boost the immunotherapy efficiency, Adv. Sci. 9 (22) (2022) e2201734, https://doi.org/10.1002/advs.202201734.

[67] H. Ma, Y. Lu, Z. Huang, S. Long, J. Cao, Z. Zhang, X. Zhou, C. Shi, W. Sun, J. Du, J. Fan, X. Peng, ER-targeting cyanine dye as an NIR photoinducer to efficiently trigger photoimmunogenic cancer cell death, J. Am. Chem. Soc. 144 (8) (2022) 3477–3486, https://doi.org/10.1021/jacs.1c11886.

[68] R. Alzeibak, T.A. Mishchenko, N.Y. Shilyagina, I.V. Balalaeva, M.V. Vedunova, D. V. Krysko, Targeting immunogenic cancer cell death by photodynamic therapy: past, present and future, J Immunother Cancer 9 (1) (2021), https://doi.org/10.1136/jitc-2020-001926.

[69] G. Mestrallet, K. Sone, N. Bhardwaj, Strategies to overcome DC dysregulation in the tumor microenvironment, Front. Immunol. 13 (2022) 980709, https://doi.org/10.3389/fimmu.2022.980709.

[70] D.H. Munn, V. Bronte, Immune suppressive mechanisms in the tumor microenvironment, Curr. Opin. Immunol. 39 (2016) 1–6, https://doi.org/10.1016/j.coi.2015.10.009.

[71] A. Del Prete, V. Salvi, A. Soriani, M. Laffranchi, F. Sozio, D. Bosisio, S. Sozzani, Dendritic cell subsets in cancer immunity and tumor antigen sensing, Cell. Mol. Immunol. 20 (5) (2023) 432–447, https://doi.org/10.1038/s41423-023-00990-6.

[72] X. Peng, Y. He, J. Huang, Y. Tao, S. Liu, Metabolism of dendritic cells in tumor microenvironment: for immunotherapy, Front. Immunol. 12 (2021) 613492, https://doi.org/10.3389/fimmu.2021.613492.

[73] Z. Hu, L. Ye, Y. Xing, J. Hu, T. Xi, Combined SEP and anti-PD-L1 antibody produces a synergistic antitumor effect in B16-F10 melanoma-bearing mice, Sci. Rep. 8 (1) (2018) 217, https://doi.org/10.1038/s41598-017-18641-y.

[74] J. Ding, H. Xiao, X. Chen, Advanced biosafety materials for prevention and theranostics of biosafety issues, Biosaf Health 4 (2) (2022) 59–60, https://doi.org/10.1016/j.bsheal.2022.03.011.

[75] Y. Yu, J. Ding, Y. Zhou, H. Xiao, G. Wu, Biosafety chemistry and biosafety materials: a new perspective to solve biosafety problems, Biosaf Health 4 (1) (2022) 15–22, https://doi.org/10.1016/j.bsheal.2022.01.001.

[76] M. Amiri, O. Molavi, S. Sabetkam, S. Jafari, S. Montazersaheb, Stimulators of immunogenic cell death for cancer therapy: focusing on natural compounds, Cancer Cell Int. 23 (1) (2023) 200, https://doi.org/10.1186/s12935-023-03058-7.

[77] W. Wang, F. Yang, L. Zhang, M. Wang, L. Yin, X. Dong, H. Xiao, N. Xing, Targeting DNA damage and repair machinery via delivering WEE1 inhibitor and platinum (IV) prodrugs to stimulate STING pathway for maximizing chemo-immunotherapy in bladder cancer, Adv. Mater. 36 (1) (2023), https://doi.org/10.1002/adma.202308762.

[78] K.N. Kodumudi, J. Siegel, A.M. Weber, E. Scott, A.A. Sarnaik, S. Pilon-Thomas, Immune checkpoint blockade to improve tumor infiltrating lymphocytes for adoptive cell therapy, PLoS One 11 (4) (2016) e0153053, https://doi.org/10.1371/journal.pone.0153053.